ENERGY-RELATED RESEARCH IN THE DOE OFFICE OF BASIC ENERGY SCIENCES

Patricia M. Dehmer

Office of Basic Energy Sciences, U. S. Department of Energy, SC-10/Germantown Building, 1000 Independence Avenue, SW, Washington, DC 20585-1290

The $1 billion Basic Energy Sciences (BES) program in the Department of Energy's Office of Science sponsors fundamental research in materials sciences and engineering, chemistry, geosciences, and biosciences that impacts energy resources, production, conversion, efficiency, and the mitigation of the adverse impacts of energy production and use. BES supports a large extramural research program, with approximately 40% of the program's research activities sited at academic institutions. BES also plans, constructs, and operates major scientific user facilities, including synchrotron radiation light sources, neutron scattering facilities, electron-beam microcharacterization centers, nanoscale science research centers, and facilities for materials synthesis and processing.

Dr. Patricia Dehmer, Director of BES, will give an overview of emerging research opportunities including summaries of three recent workshops that will shape the future course of the program – *Basic Research Needs for a Secure Energy Future*, *Basic Research Needs for the Hydrogen Economy*, and *A 20-year Basic Energy Sciences Facilities Roadmap*. Specifically, she will highlight BES' priorities related to the Administration's Hydrogen Fuel Initiative and the BES-sponsored hydrogen workshop report.

BASIC RESEARCH NEEDS FOR THE HYDROGEN ECONOMY

Mildred S. Dresselhaus

Massachusetts Institute of Technology, 77 Massachusetts Avenue, Cambridge, MA 02139

A summary is presented of a recent BES/DOE sponsored report that addresses the basic research needs in the areas of hydrogen production, storage, and use in fuel cells that would be necessary to bridge the large gap between present scientific knowledge/technical capabilities and what would be required for the practical realization of a hydrogen economy. In this report, research opportunities that might be effective in bridging this gap are identified in the areas of advanced materials (especially nanostructured materials), catalysis, modeling and simulations, bio-inspired approaches, and interdisciplinary efforts.

BASIC RESEARCH NEEDS IN HYDROGEN PRODUCTION FOR A HYDROGEN ENERGY ECONOMY

Thomas E. Mallouk[1] *and Laurens Mets*[2]

[1]Department of Chemistry, 152 Davey Laboratory, The Pennsylvania State University, University Park, PA 16802

[2]Department of Molecular Genetics and Cell Biology, University of Chicago, 1103 E. 57th St, Chicago, IL 60637

We report the findings on hydrogen production from a recent Department of Energy sponsored workshop on hydrogen production, storage, and use. The development of large scale, cost-effective, and sustainable hydrogen production methods poses many technical challenges. We consider basic research needs in the context of the scale of the problem, current methods of hydrogen production, and the timeline for implementation of hydrogen as an energy currency for transportation and other uses.

HYDROGEN STORAGE ISSUES IN A NEW HYDROGEN ECONOMY

Puru Jena

Physics Department, Virginia Commonwealth University,
Richmond, Virginia 23284-2000

The limited supply of fossil fuels, its adverse effect on the environment, and growing worldwide demand for energy has necessitated the search for new and clean sources of energy. The possibility of using hydrogen to meet this growing energy need has rekindled interest in the study of safe, efficient, and economical storage of hydrogen. Unfortunately, the current methods for storing hydrogen as a compressed gas or liquid do not meet the industry requirements. An alternate method for hydrogen storage involves metal hydrides. The conventional intermetallic hydrides store hydrogen at interstitial sites and are reversible at around room temperature. However, the relative weight of stored hydrogen in these materials is rather low (1 – 3 wt %) and do not meet the requirement of the transportation industry (~10 wt %). A novel approach for hydrogen storage is to combine the favorable kinetics and thermodynamics of conventional metal hydrides with that of the large hydrogen storing capacity of organic molecules such as CH_4. Although alanates, with the chemical composition $[M^{n+} (AlH_4)^{n-}$, M= Li, Na, K, Mg], belong to this class, the desorption temperature of hydrogen in these materials is rather high. It was recently discovered that doping of Ti-based catalyst in $NaAlH_4$ can significantly lower the hydrogen desorption temperature, but why and how Ti accomplishes this task remains a mystery. Using first principles calculations, we will provide a molecular level understanding of the role of Ti in lowering the hydrogen desorption temperature in $NaAlH_4$ and $LiBH_4$. It is hoped that the understanding gained here can be useful in designing better catalysts as well as hosts for hydrogen storage.

FUEL CELLS: THE FINAL STEP IN A HYDROGEN ECONOMY

Francis J. DiSalvo

Department of Chemistry and Chemical Biology, Cornell University, 102 Baker Laboratories, Ithaca, NY 14853

Fuel Cells transform the chemical energy carried by a fuel into electrical energy. Hydrogen fuel cells are especially well suited for this task because they operate with high efficiency, they do not produce pollution, and they provide electrical power that can be tailored to a wide variety of applications – from large stationary power plants to transportation vehicles to consumer devices like cell phones and personal computers – all assuming that the challenges of hydrogen production and storage can be met.

The basic fuel cell types span a remarkable range of operating temperatures, construction materials, and performance specifications. Although fuel cells offer many advantages for a diverse set of applications, so far they have been introduced only on a limited scale and at high cost. There are serious and difficult obstacles to widespread implementation of fuel cell technology. Most of the challenges arise from the need for inexpensive, more durable materials that also have better operating characteristics, especially in the case of the electrocatalysts, membranes (ionic conductors) and reformer catalysts.

Reformers offer the potential for operating fuel cells by using a range of primary fuels based on gaseous or liquid hydrocarbons. Some current and proposed fuel cell power systems that are capable of using fuels other than hydrogen, either directly or through reformers, may serve as transitional technologies along the path to a full hydrogen economy. These hydrocarbon-based fuel cells may be important in increasing the efficiency of fuel use and in decreasing emissions or noise, a highly valued aspect in some military, commercial and consumer applications in the shorter term. However, some of the fundamental problems in fuel cell technology are independent of the fuel source, as we will discuss in this presentation.

In this presentation, we discuss primarily the challenges and problems associated with low-temperature fuel cells (operating from 40 to 150 or 200 ^{o}C) and, to a lesser extent, with high-temperature (650 to 1000 ^{o}C) fuel cells. Low temperature fuel cells, in particular, are the focus of current automotive fuel cell R&D activities that, when implemented, would be a major component of a hydrogen economy.

The development of efficient, durable and low cost fuel cells is a grand challenge that will take substantial and sustained efforts in chemical and materials research. These challenges can only be met by new materials with improved, or even revolutionary, properties and performance. A basic, exploratory research program of significant size and scope is needed to produce these enabling discoveries.

This presentation will outline many of the challenges and opportunities that need to be addressed with basic research in materials synthesis, analytical studies of the processes and kinetics of reaction as well as materials degradation, theoretical modeling, etc. It is hoped that by outlining the challenges, the scientific community can be energized to be engaged in the process of discovery and invention to produce the breakthroughs necessary to enable this vision of an energy future that promises less pollution and less reliance on energy imports.

THE PRESIDENT'S HYDROGEN FUEL INITIATIVE

Steve Chalk, Pat Davis, Pete Devlin, JoAnn Milliken, and John Petrovic

Office of Hydrogen, Fuel Cells and Infrastructure Technologies, U.S. Department of Energy, 1000 Independence Avenue SW, Washington, DC 20585

In his 2003 State of the Union address, President Bush launched the Hydrogen Fuel Initiative, "so that America can lead the world in developing clean hydrogen-powered automobiles". The elements of this Initiative involve research, development and demonstration activities on hydrogen production and delivery, hydrogen storage, fuel cells, technology validation, safety, codes/standards, and education. The DOE-OHFCIT goals and objectives for each of these aspects will be described. Research and development needs and opportunities in chemistry and materials science related to hydrogen production, storage, and fuel cells will be highlighted. The Hydrogen Fuel Initiative will provide the RD&D necessary or a decision in 2015 by U.S. industry to commercialize fuel-cell-powered vehicles.

Efficient Bimetallic Catalysts for the Hydrogen Production from Diesel fuel

Praveen K Cheekatamarla and Alan M. Lane

Department of Chemical Engineering, The University of Alabama, Tuscaloosa, AL-35487

Introduction

Autothermal reforming involves the reaction of oxygen, steam, and fuel to produce H_2 and CO_2. In essence, this process can be viewed as a combination of POX and SR and has recently attracted considerable attention due to its higher energy efficiency than the above processes and also low investment process using a simple system design [1]. The ATR is a stand-alone process in which the entire hydrocarbon conversion is carried out in one reactor aided by partial oxidation. The ATR process is generally defined by an idealized equation written as:

$C_nH_mO_p + x(O_2+3.76N_2) + (2n -2x-p)H_2O = nCO_2 + (2n-2x-p+m/2)H_2 + 3.76xN_2$

where, x is the oxygen-to-fuel molar ratio. When x = 0 equation reduces to the endothermic steam reforming; when x = n-p/2 equation is the combustion reaction.

ATR has several advantages over SR and POX: (1) less complicated reactor design and lower reactor weights, because less thermal integration (i.e. heat exchange between incoming reactants and the hot products) is required; (2) a wider choice of materials of construction; and (3) lower fuel consumption during startup because, for a given reactor mass, the energy required to heat a reformer is directly proportional to its operating temperature.

In the past, various fuels have been investigated for H_2 generation by reforming technologies for fuel cell systems. Suitable fuels involved gaseous HCs such as methane, propane etc. [2] and liquid HCs such as alcohols [3], gasoline [4, #2 diesel [5] etc.

For heavy fuels such as JP-8 or kerosene, autothermal reforming conditions were achieved by using a reformer including a POX zone and a separate SR zone. The operating conditions were maintained such that oxygen (air) was preheated to 450°C, and the temperature of POX chamber and SR chamber maintained at 1375°C and 925°C respectively [6]. It is also reported that in the autothermal reforming of the diesel feed, the thermodynamic equilibrium can be achieved at a Water/C of 1.25 and an oxygen/C ratio of 1 at an operating temperature of 700°C [7].

Although considerable work was done on heavy hydrocarbons, there haven't been any studies related to synthetic diesel fuel and the performance of adiabatic reactors for autothermally reforming the fuel.

The design of ATR catalysts can be challenging, particularly for gasoline/diesel reforming due to the complex and ill-defined nature of the fuel. ATR catalysts have to be active for both steam reforming and partial oxidation, be robust at high temperature and resistant to sulfur and coke formation, especially in the catalytic zone that runs oxygen limited.

Full conversion of all hydrocarbon components is desired; low levels of non-methane hydrocarbons, such as aromatics and olefins can undergo transformations, particularly hydrogenation on the downstream WGS catalyst, thus consuming hydrogen and decreasing the overall efficiency of the fuel processor.

Catalyst formulations for ATR fuel processors depend on the fuel choice and operating temperature. For methanol, Cu-based formulations can be used. For higher hydrocarbons the catalyst typically comprises of metals such as Pt, Rh, Ru and Ni deposited or incorporated into carefully engineered oxide supports such as ceria-containing oxides.

The objective of this investigation was to synthesize and test stable and efficient autothermal reforming catalysts for hydrogen production in auxiliary power units.

Experimental

All the experiments were performed in a 3/8" adiabatic fixed-bed tubular (quartz) reactor. Liquid feed consisting of water and diesel was vaporized and mixed along with air in a pre-heater containing silicon carbide bed to enhance mixing and heat transfer. Calibrated HPLC pumps and unit mass flow controllers were used to control the flow rates. The gaseous mixture from the pre-heater was maintained at a temperature of 400°C. The reactor with the catalyst bed was well insulated to achieve adiabatic reaction conditions. Thermocouples were placed along the catalytic bed to read the temperature profile inside the reactor as the reactions occur over the catalytic surface and the corresponding product composition was measured by sampling at different positions. The hot product gas leaving the reactor was cooled down in a heat exchanger/condenser system to separate water and liquid hydrocarbons from the product gas. The pressure was always less than 2 psig. The dry product gas from the condenser was analyzed using a SRI gas chromatograph to monitor H_2, CO, CO_2, CH_4 and O_2 concentrations.

In each test, 2 g of fresh non-diluted catalyst sample (pellets with an average size of 2 mm) was supported on a layer of quartz wool. The catalysts tested for the ATR activity were prepared by impregnation and co-impregnation techniques.

The experiments reported in this document were performed under the following conditions: Steam/C ratio = 1-3, oxygen/C ratio = 0.5-2, pre-heater and reactor inlet temperature = 400°C, Space Velocity = 17000 hr^{-1}.

Results and Discussion

The role of defect chemistry and the surface oxygen vacancies in determining the catalytic behavior of metal supported mixed oxide systems is well known. The focus was on the autothermal reforming activity of some catalysts, as well as, the effect and role of both the metal and the dopant on the catalytic properties. The experimental work involved developing, testing and characterizing: (a) single metal catalysts supported on reducible or non-reducible support; (b) bimetallic catalysts dispersed on various supports. Reactor studies involved the reforming of synthetic diesel fuel. Catalysts were prepared by impregnation, incipient wetness method and coprecipitation. Metal loadings generally range from 1-2% in the case of noble metals and 5-10% for non-noble metals.

Alumina supported catalysts

The main objective of the present work was to determine whether the autothermal reforming activity of Pt can be improved when a second noble metal (Pd) is added to the alumina substrate. This carrier was selected because of its non-reducible nature, as a part of fundamental study to better understand the performance of autothermal reforming catalysts: metals and metal oxides.

Three model samples were prepared to study the ATR activity of synthetic diesel fuel: Pt, Pd and Pt-Pd catalysts supported on alumina. Two different bimetallic samples were prepared by changing the order of impregnation: Pt (I)-Pd (II); Pd (I)-Pt (II).

The autothermal reforming activity response of alumina supported Pt and/or Pd catalysts is shown in Fig. 1. Before carrying out the activity tests, all the samples were reduced at 350°C in a 5%H_2/N_2 mixture. Samples loaded with Pt or Pd yielded about 50%

hydrogen compared to 45% from bare alumina. The most interesting results are obtained from the mixed metal bimetallic catalysts, the Pt-Pd samples. Each bimetallic sample shows high activity yielding ~60% hydrogen compared to 50% from their monometallic counterparts. The order of impregnation does not seem to have any impact on the performance of these catalysts as noted in the figure. The ATR activity on the Pt, Pd and Pt-Pd catalysts confirms a positive effect of Pt and Pd in the bimetallic sample, because the level of activity of this system was higher than on either of the monometallic components.

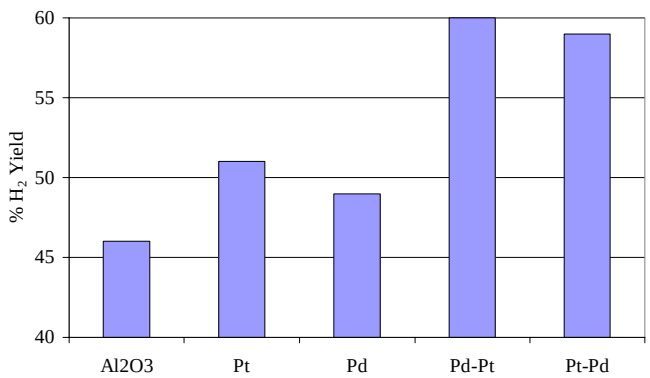

Figure 1. Performance of alumina supported Pd and/or Pt catalysts

This higher intrinsic activity of these catalysts is probably due to the Pt-Pd interaction in the system. Temperature programmed reduction studies and XPS analysis confirmed the expected phenomenon.

TPR profiles of monometallic (Pd and Pt) and the bimetallic (Pt followed by Pd) samples are shown in Fig. 2. TPR pattern of alumina carrier is not shown because of its non-reducible nature.

The TPR profile (Fig. 2) of the Pd sample shows a negative peak at 75°C followed by a positive peak at 110°C. The former can be assigned to desorption of hydrogen from the decomposition of a bulk palladium hydride formed through H-diffusion in to the Pd-crystallites [214], while the latter is attributed to the Pd oxide species. In contrast, the TPR profile of the Pt sample shows a broad reduction profile extending from 50°C to 450°C. All platinum is reduced to Pt metal below 450°C. Two reduction peaks one at about 100°C and the other at 250°C were observed for Pt/Al_2O_3. The broadening suggests the presence of several Pt species. These reduction peaks are slightly lower than the reported reduction temperature [8] probably due to differences in Pt loading, alumina type, calcination temperature and ramp rates during the TPR.

The TPR profile of the bimetallic Pt-Pd catalyst is not simply the sum of the monometallic Pt and Pd samples. The bimetallic reduction profile exhibits peaks typical of PtO reduction (100°C) and PdO (110°C) in addition to the Pd hydride decomposition peak at 75°C, although both are much more intense than in the monometallic samples. Since the metal content is about the same in these catalysts, the increase in H_2 consumption associated with the metal oxide species seems to depend on the presence of second metal. In addition, the broader second peak centered at 400°C, detected in the Pt-Pd sample indicates the reduction of Pd species together with the co-impregnated Pt, probably due to some kind of interaction between the metals. Similar interactions in Pt-Pd systems were reported in TPR studies performed by Noronha et al. [9]. These interactions between the metals leading to the formation of an active phase seem to be a probable reason behind the activity enhancement.

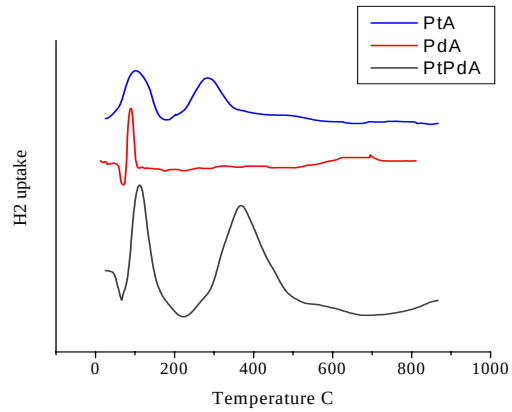

Figure 2: TPR Profiles of alumina supported catalysts

The XPS analysis performed over these samples verify the above conclusions. The high resolution XPS spectra of the Pt 4d and the Pd 3d binding energy regions obtained from the Pt/Al_2O_3, Pd/ Al_2O_3 and Pt/Pd/ Al_2O_3 samples are shown in Fig. 4-48a. Note a slight shift in the Pd 3d5/2 peak (~0.5 eV to higher binding energy) of the Pt-Pd/Al_2O_3 catalyst with respect to that of the Pd/ Al_2O_3 catalyst. The shift in the Pd 3d5/2 peak may be due to the formation of stabilized Pd species due to a strong metal-metal interaction between Pd and Pt in the bimetallic sample.

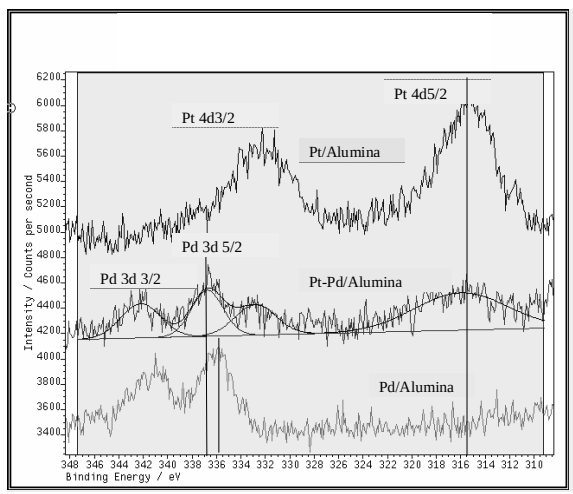

Figure 3: XPS analysis of alumina supported catalysts

Ceria Supported Catalysts.

Two different metals viz. Pt, Ni were chosen for their ATR activity. The ceria supported catalysts include monometallic components and their combinations with Pt (Pt-Ni). Two different bimetallic samples were also prepared by changing the order of impregnation on ceria substrate. It can be noted from Fig. 4 that these metals improved the ATR activity of ceria support. Similar to the

results observed over the alumina supported catalysts discussed in the above section, the selectivity to produce hydrogen from diesel fuel was highest for the bimetallic samples compared to their monometallic counterparts. The impregnation order clearly had an effect on the activity in case of the Pt-Ni bimetallic catalysts as observed in Fig. 4. Also these catalysts exhibited stable performance showing almost complete resistance to sulfur poisoning. A long-term experiment was carried out over these catalysts (Pt, and Pt-Ni). It is clear from Fig. 5 that the bimetallic sample shows stable catalytic activity even in presence of heavy sulfur content due to the JP8 fuel in the ATR tests conducted. The reason for this higher intrinsic activity and stability is underway.

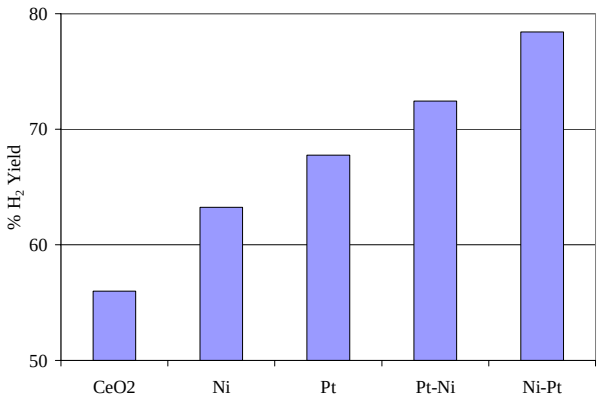

Figure 4: ATR activity of Ceria supported Pt and/or Ni catalysts

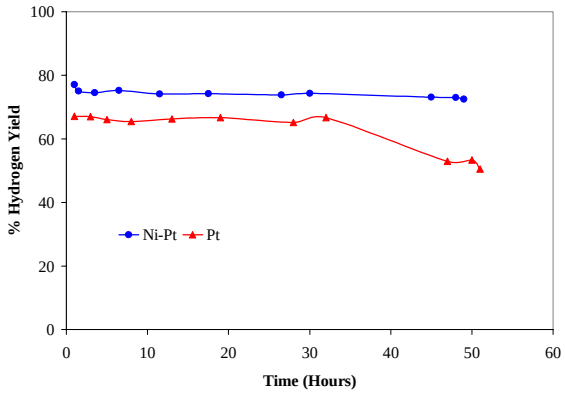

Figure 5: ATR activity (Sulfur resistance) Pt-Ni catalyst

Conclusions

Autothermal reforming of synthetic diesel fuel was investigated for potential applications in auxiliary power units. Experimental results suggest that the presence of a second metal improves the performance of the ATR activity of Pt based catalysts supported on ceria and alumina. Higher intrinsic activity of these samples is possibly due to the interaction between these metals as suggested by TPR and XPS results.

References

(1) Wieland S.; Baumann F.; Startz K.A.; "Proceedings of the fuel cell seminar on new catalysts for autothermal reforming of gasoline and water-gas shift reaction" *Portland, Oregon*, **2000**.

(2) Ayabe S.; Omoto H.;T. Utaka, R.; Eguchi K.; *Applied Catalysis A: General* **2002**, *6352*, 1

(3) Ahmed S.; Krumplet M.; Kumar R.; Lee S.H.D.; *Presented at the Fuel Cell Seminar, Palm Springs, California*, **1998.**

(4) Dong J Moon, Sreekumar K.; Sang Deuk Lee and Hoon Sik Kim, *Applied Catalysis A: General* **2001,** *215*, 1

(5) Pereira C.; Bae J-M.; Ahmed S.; and Krumplet M.; Presented at the US Dept. of Energy, 2000 Hydrogen Program technical review, San Ramon, CA**, May 2000**.

(6) "Apparatus for converting hydrocarbon fuel in to hydrogen gas and carbon dioxide",*US Patent 6254839*.

(7) Thomas Rampe Angelika Heinzel and Bernhard Vogel, *Journal of Power sources* **2000**, *86*, 536.

(8) Lietz, G.; Lieske, H.; Spindler, H.; Hanke,W.; and Wolter, J.; *J. Catal*. **1983**, *81*, 17

(9) Noronha, F. B.; Schmal, M.; Primet, M.; and Fr ety R.; *Appl. Catal*., **1991**, *78*, 125

PARAMETRIC STUDY OF AUTOTHERMAL REFORMING OF LPG

Wuyin Wang, Scott Q. Turn, Vheissu Keffer, Aurelien Douette

Hawaii Natural Energy Institute,
University of Hawaii,
1680 East-West Road, POST 109,
Honolulu, HI 96822
Email: Wuyin@hawaii.edu;
Tel: 808-956-5397; Fax: 808-956-2344

Introduction

Generating electricity by fuel cell technologies is under extensive research recently with a potential for commercialization in the near future. Sources of hydrogen for fuel cell are diverse and fuel processing is a key part to ensure reliable performance and competitive economy of fuel cell applications. Conventional hydrocarbon fuels are cheap and widely available. In Hawaii, the majority of electricity is generated from fossil fuels. There are ample supplies of Liquid Petroleum Gas (LPG) and its price is competitive to that of gasoline. Being safe and non-toxic, LPG is a promising source of hydrogen for off-grid applications in Hawaii.

Hydrocarbon fuels can be converted into high quality hydrogen for PEM fuel cells through reforming, water-gas shift reaction, and CO cleanup. Steam reforming, catalytic partial oxidation and autothermal reforming are the main processes employed to convert hydrocarbons to hydrogen rich gas. Compared with natural gas, LPG, mainly propane, contains C-C bonds that will be broken at higher temperature.

Coking is a main cause of catalyst failure in hydrocarbon reforming. Carbonaceous deposits on catalyst surfaces block active sites, leading to catalyst deactivation. Coke formation from thermal cracking can accompany catalytic reforming above approximate 650°C [1]. Therefore for LPG reforming at high temperature, coking must be carefully controlled.

Ethyl mercaptan is commonly added to LPG as an odorant. Ethyl mercaptan will mainly be converted to hydrogen sulfide in autothermal reforming. For steam reforming catalysts, sulfur will readily bind with nickel causing severe deactivation. The effects of sulfur on catalyst activity are weaker at high temperature and correlate with sulfur concentration in the feedstock [2].

This paper reports preliminary results from a parametric study of autothermal reforming of LPG. Reforming temperature, steam to carbon ratio (S/C), and oxygen to carbon ratio (O/C) were studied. Performance indicators, the extent of LPG conversion and catalyst coking, and sulfur poisoning, are reported.

Experimental

Experiments were performed in a 1.93 cm I.D. tubular reactor. The reactor was heated by electrical furnace with a heating length of 30.5 cm. Two G90 steam reforming catalysts, G-91 EW and C11-NK, from Süd-Chemie were tested. The LPG supply contained 90-100% propane/propylene, 0-2% ethane, 0-10% butane and 40 ppm ethyl mercaptan.

A stream of 2 slpm air was fed into a water vaporizer to produce a steady flow with steam. When temperatures in the reactor reached desired set point values, LPG was introduced and the gas mixture was switched from a bypass mode to the catalyst reactor. Air and LPG flow rates were maintained using mass flow controllers. About 20 to 40 g catalyst were located in the constant temperature zone in the reactor. Temperatures in the reactor were measured at three locations, 7.5 cm in front of the catalyst bed (T1), directly in front of the catalyst bed (T2) and immediately after the catalyst bed (T3). The dry effluent gas was analyzed using a Shimadzu GC 14A equipped with a Carbonex packed column and a thermal conductivity detector. The gas components H_2, N_2, CO, CH_4, CO_2, C_2H_4, C_2H_6, C_3H_6 and C_3H_8, were quantified.

Catalyst temperature, S/C, O/C and catalyst mass (i.e. space velocity) were studied at 2-3 levels. Both steam reforming and autothermal reforming were investigated. Steam-to-carbon ratio was 0.6 or 1.5. Oxygen-to-carbon ratio was 0.76 or 1.0. The amount of catalysts was 20 or 40 g. Temperature of the reformer was set at 680, 770, 850°C. Real temperatures in the reactor were shown by T1, T2 and T3. Temperature at the end of the catalyst bed, T3 was used to represent the catalytic reactor temperature.

Results and Discussion

Catalyst. Two catalysts tested are designed for different feed stocks, G91 EW for natural gas/LPG and C11-NK for naphtha. Both catalysts showed similar activity in LPG conversion, however, G91 EW was more active in converting methane and ethylene (Table 1) under the conditions tested. Since the amount of catalyst was in excess, the influence of catalyst type on hydrocarbon conversion was weak in the test range.

Table 1. Gas Compositions after Reforming by Two Catalysts. S/C=1.5, O/C=1.0, T3=800°C, GHSV=9000 1/h.

%	H_2	N_2	CO	CH_4	CO_2	C_2H_4	C_3H_8
C11 NK	33	46	11	1.4	9.3	0.38	0
G91 EW	35	45	11	0.24	8.7	0.06	0

Temperature. Temperature of the catalyst bed was the most important factor for LPG conversion. Complete conversions of C_3H_8 and C_3H_6 was achieved at catalyst bed temperature of 840°C (average of T2 and T3), at S/C=1.5 and O/C=1.0 (Table 2).

Table 2. Effect of Temperature on Propane Conversion. S/C=1.5, C11-NK 42 g, O/C=1.0.

T bed, °C	704	725	840
C_3H_8 conversion, %	98.5	98.7	100

O/C ratio. In autothermal reforming, the role of oxygen is to provide heat required to drive steam reforming reactions and to break fuel into smaller compounds. At high O/C ratio, the chemical energy of fuel may be converted to sensible heat rather than the desired H_2 product. At low O/C ratio, coke may form due to thermal cracking of hydrocarbons. In the present work, O/C ratio of 1.0 was chosen since experience indicated that coke formation was generally lower at this condition. This ratio was equal to about 30% of oxygen needed for complete combustion of propane. In gasification research, this O/C ratio was usually found to be optimal. Further experiments are planned to quantify the effects of O/C ratio on system performance.

S/C ratio. In autothermal hydrocarbon reforming, partial oxidation reactions occur faster than steam reforming reactions. Since partial oxidation is very exothermic while steam reforming is extremely endothermic, the occurrence of these two sets of reactions can be deduced from the temperature profile in the reactor (Figure 1). The "No LPG" curve indicates that flow through the reactor does not reach the furnace control set point temperature of 770ºC until close the location of x/L=0.5. Compared with this, low S/C ratios of 0.6 and 1.0 resulted in high temperature before the catalyst bed indicating that heat released from oxidation (O/C=1.0) dominated the heat demand of the steam reforming reactions. At S/C ratio of 1.5,

enhanced steam reforming reactions result in lower temperatures at the entrance of the reactor (x/L=0.25). All three S/C ratios have roughly equal temperatures (~850ºC) in excess of the furnace temperature set point at x/L=0.5 indicating the heat release by the oxidation is dominant at this location. Differences in total flow rate through the reactor are not accounted for in this discussion.

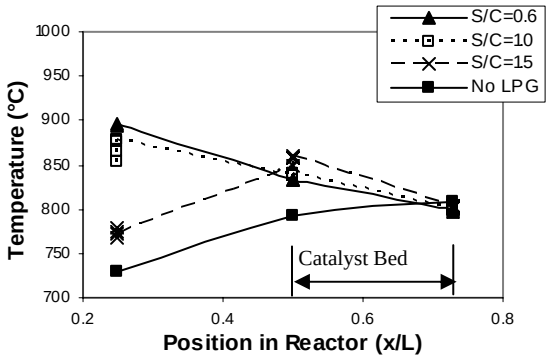

Figure 1. Influence of S/C on temperatures in the reactor. L: total heated reactor length, x: distance from inlet in the reactor. T3=800°C, O/C=1.0, G91 EW: 22 g.

Steam reforming was slow and was kinetically controlled (Figure 2). Though propane and propylene were completely converted, methane levels in the effluent were higher than values predicted by equilibrium calculations. Concentration of ethylene, a precursor of coking, was low. Both methane and ethylene decreased with increasing S/C ratio.

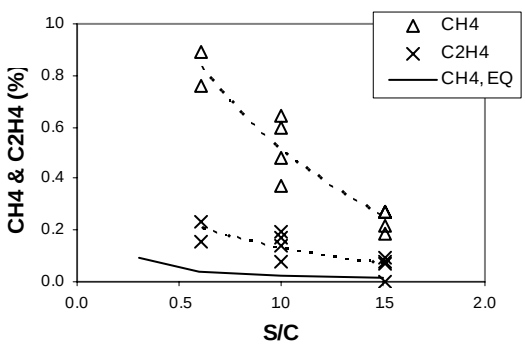

Figure 2. Effect of S/C ratio on methane and ethylene. Equilibrium value for methane is given for comparison. T3=800°C, O/C=1.0, G91 EW:22 g, GHSV=9000 1/h.

S/C ratio affected conversions of C_3H_8 and C_3H_6 to some extent. Trace amount of C_3H_8 was detected at 800°C (T3) when S/C and O/C were lowered to 1.1 and 0.76, respectively.

The choice of a proper S/C ratio should also take into account energy balance of the reformer system. Equilibrium calculations indicate that with preheating of inlet gas by exhaust gas, autothermal reforming could be operated without external heat supply at S/C=1.5 and O/C=1.0.

Deactivation of the catalyst. Autothermal reforming of LPG was tested for more than 40 hours under conditions of S/C=1.5, O/C=1.0, GHSV=9000 1/h, and a reactor set point temperature of 770°C. The gas compositions are plotted in Figure 3. Under these conditions, gas composition was generally stable. No propane or propylene was detected. Hydrogen declined slightly with increasing time on stream. Methane increased considerably, which was a sign of catalyst deactivation. Ethylene increased as well, and ethane started to appear after 35 hours on stream.

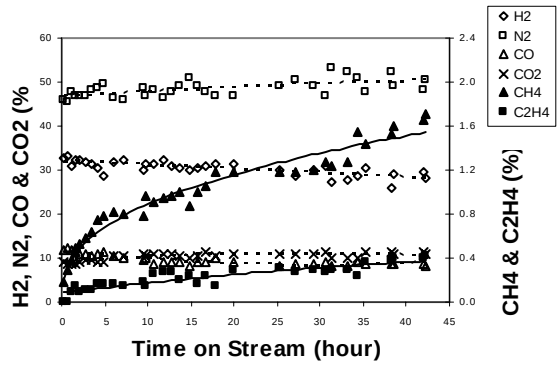

Figure 3. Autothermal reforming of LPG. T3=800°C, S/C=1.5, O/C=1.0, G91 EW: 23 g, GHSV=9000 1/h, ethyl mercaptan in LPG: 40 ppm.

Upon visual inspection at the conclusion of the test, the first piece of the catalyst in the catalytic bed was discolored, indicating partial oxidation was dominant at that point. No clear carbon deposition on the used catalyst was evident. With 40 ppm sulfur in LPG, sulfur poisoning was the likely cause of deactivation due to the formation of nickel sulfide on the active sites of the catalyst surface. More detailed analysis of sulfur on the catalyst surface is expected to be obtained soon.

Conclusions

Effects of different parameters on autothermal reforming of LPG were studied for hydrogen production. Two nickel-based G90 steam reforming catalysts were used. Experiments were carried out in a fixed-bed reactor to study the effects of catalyst type, reforming temperature, S/C ratio, and O/C ratio. Temperature was found to be most important. Complete conversion of LPG was achieved above 800°C (T3). Higher S/C ratio (S/C=1.5) resulted in the reduced levels of methane and ethylene. Controlling O/C and S/C, heat for steam reforming could be provided by partial oxidation in situ and C3 hydrocarbons could be partially oxidized to smaller molecules with less thermal cracking. Finally, autothermal reforming of LPG was tested by more than 40 hours on stream at S/C=1.5, O/C=1.0, 800°C and GHSV=9000 1/h. The propane conversion remained complete, but a slight drop of methane conversion was observed. No clear carbon deposit was found. The deactivation was probably due to poisoning by 40 ppm sulfur from LPG feed.

References

(1) Rostrup-Nielsen, J.R., *Catalysis Today*, **1997**. *37*, 225-232.
(2) Rostrup-Nielsen, J.R., *Catalytic Steam Reforming*, in *Catalysis: Science and Technology*, J.R. Anderson and M. Boudart, Editors. 1984, Springer-Verlag: Berlin. pp. 1-117.

COMPARISON OF AUTOTHERMAL REFORMING FOR HYDROCARBON FUELS

Bijan F. Hagh

ES Logic, LLC
4231 E. Regency Avenue
Orange, CA. 92867

Introduction

The development of fuel cells is promised to enable the distributed generation of electricity in the near future. However, the infrastructure for production and distribution of hydrogen, the fuel of choice for fuel cells, is currently lacking. Efficient production of hydrogen from fuels that have existing infrastructure (e.g., natural gas or gasoline) would remove a major roadblock for acceptance of fuel cells for distributed power generation.

There are a number of fuel processing technologies for hydrogen generation from hydrocarbon fuels, but in actuality these technologies are points along a spectrum that spans combustion and partial oxidation (POX) through steam reforming (SR) (1). Autothermal reforming (ATR) combines partial oxidation (POX) and SR, in a single process. POX reaction is exothermic or produces heat, while SR reaction is endothermic and heat must be generated external to the reformer process. Other exothermic reactions that may simultaneously occur in ATR include water gas shift (WGS) and methanation reactions. Typically, ATR reactions are considered to be thermally self-sustaining, and therefore, do not produce or consume external thermal energy. Catalysts are commonly used to enhance the reaction rate of the reforming processes at lower temperatures.

Independent parameters that affect the performance of an ATR reactor are inlet feed temperature, steam-to-carbon ratio (S/C), oxygen-to-carbon ratio (O_2/C), and pressure. S/C and O_2/C are defined as the ratio of H_2O and O_2 feed to the reaction relative to carbon in the fuel on a molar basis respectively. Dependent parameters include reformate outlet temperature, conversion and reactor heat loss.

In this study, a general framework for comparison of fuel reforming data, in the full range of steam reforming to combustion, is developed based on stoichiometric analysis of autothermal reforming. This framework is then applied to determine the reforming reaction space for various hydrocarbons fuels. H_2 yield from fuel processing is determined based on energy and material balance coupled with chemical equilibrium requirements. The assumptions inherent in the ATR energy and material balance are as follows:

- Complete consumption of O_2 without formation of carbon soot, which is a reasonable assumption at a S/C level of 2 or above (2).
- The carbon in the fuel is reformed to CH_4, CO or CO_2 only. For reforming of methane, CO and CO_2 constitute the only carbon containing reforming products (3).
- SR, WGS and methanation (for non-methane fuels) reactions are assumed to be at equilibrium at ATR outlet temperature. This is again a reasonable assumption based on previous studies (4).
- Adiabatic reaction

Generalized Reforming Reaction Space

ATR reaction stoichiometrics for a generalized fuel, $C_xH_YO_Z$, can be represented as:

$$C_xH_YO_Z + a\,O_2 + b\,H_2O = c\,CH_4 + d\,CO + e\,CO_2 + f\,H_2$$

Where,

Table 1 - Fuel Properties

Fuel - $C_XH_YO_Z$	X	Y	Z	Max Yield = (y/2)+2x-z	$\Delta°H_f$ (kJ/mole) @ 25°C	LHV (kJ/mole)
Hydrogen	0	2	0	1	0	229.16
Methanol	1	4	1	3	-178.96	663.40
Ethanol	2	6	1	6	-203.59	1,251.96
Methane	1	4	0	4	-56.89	785.47
Propane	3	8	0	10	-66.86	2,001.89
Isooctane	8	16	0	24	-174.33	4,731.24
Dodecane	12	26	0	37	-195.10	7,392.41
Hexadecane	16	34	0	49	-248.52	9,791.77

The reference point for all enthalpies is 0 degrees absolute.

$a = O_{2,\,Feed} / C_xH_YO_{Z,Reformed}$
$b = H_2O_{Reacted} / C_xH_YO_{Z,Reformed}$
$c = CH_{4,Reformate} / C_xH_YO_{Z,Reformed}$
$d = CO_{Reformate} / C_xH_YO_{Z,Reformed}$
$e = CO_{2,Reformate} / C_xH_YO_{Z,Reformed}$
$f = H_{2,Reformate} / C_xH_YO_{Z,Reformed}$

The above assumes that all O_2 is consumed in the ATR without formation of carbon soot. Based on atomic balance for O, C and H, it can be shown that:

$b = d+2e-z-2a$
$c = x-d-e$
$f = y/2+b-2c$

Combining all three Equations and rearranging:

$$f = (y/2+2x-z) - 2a - (d+4c) \quad (1)$$

The above equation indicates that maximum theoretical hydrogen yield occurs when all the carbon in the fuel is reformed to CO_2 (i.e., no CH_4 or CO produced), which is consistent with previous literature [5]. For maximum hydrogen yield, Equation (1) reduces to:

$$f_{max} = (y/2+2x-z) - 2a \quad (2)$$

Table 1 summarizes the values of (y/2+2x-z), standard heat of formation and LHV for a number of fuels and Figure 1 shows the linear relationship between LHV and (y/2+2x-z). Defining Stoichiometric Ratio (SR) as the ratio of oxygen reacted to stoichiometric oxygen required for combustion, the maximum hydrogen yield for any fuel can be represented by the following Equation:

$$f_{max}/(y/2+2x-z) = 1 - SR \quad (3)$$

where, $SR = 2a/(y/2+2x-z)$

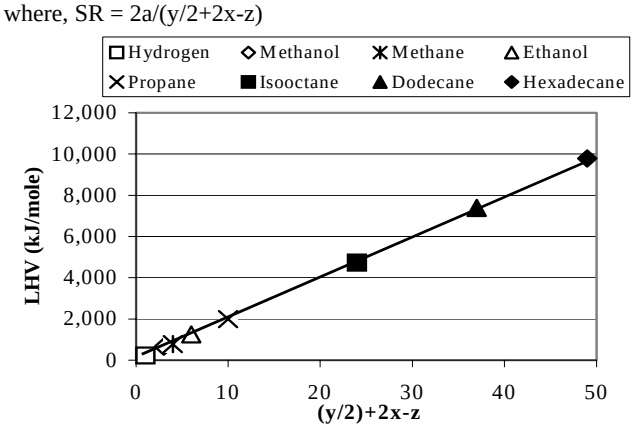

Figure 1. Maximum hydrogen yield for steam reforming of various fuels

Methane Reforming Reaction Space

ATR reaction stoichiometrics for methane fuel can be represented as:

$CH_4 + a\ O_2 + b\ H_2O = c\ CO + d\ CO_2 + e\ H_2$

Where,

$a = O_{2,\ Feed}/(CO+CO_2)_{Reformate} = (O_2/CH_4\ Feed)/X$

$b = H_2O_{Reacted}/(CO+CO_2)_{Reformate}$

$c = CO_{Reformate}/(CO+CO_2)_{Reformate} = (CO/CH_4\ Feed)/X$

$d = CO_{2,Reformate}/(CO+CO_2)_{Reformate} = (CO_2/CH_4\ Feed)/X$

$e = H_{2,Reformate}/(CO+CO_2)_{Reformate} = (H_2/CH_4\ Feed)/X$

$X = CH_4\ Conversion = (CO+CO_2)_{Reformate}/(CO+CO_2+CH_4)_{Reformate}$

The above assumes that all O_2 is consumed in the ATR without formation of carbon soot. Based on atomic balance for O, C and H, it can be shown that:

$b = e-2 = (H_2/CH_4\ Feed)/X - 2$

$c = 2-2a-b$

$d = 2a+b-1$

If $c=0$ or $CO/CO_2=0$,

$e = 4-2a$

$b = 2-2a$ or $a = 1-0.5b$

$d = 1$

The above means that a plotted versus e versus a will be straight lines. The upper solid line in Figure 2 represent the case of $CO/CO_2=0$.

If $d=0$ or $CO/CO_2=\infty$,

$e = 3-2a$

$b = 1-2a$ or $a = 0.5-0.5b$

$c = 1$

The lower solid line in Figure 2 represents the case of $CO/CO_2=\infty$. In general, it can be shown that for a given CO/CO_2 in the reformate:

$e = A-2a$

Where, $A = [3\ (CO/CO_2)+4]/[(CO/CO_2)\ +1]$

and, $3 \le A \le 4$

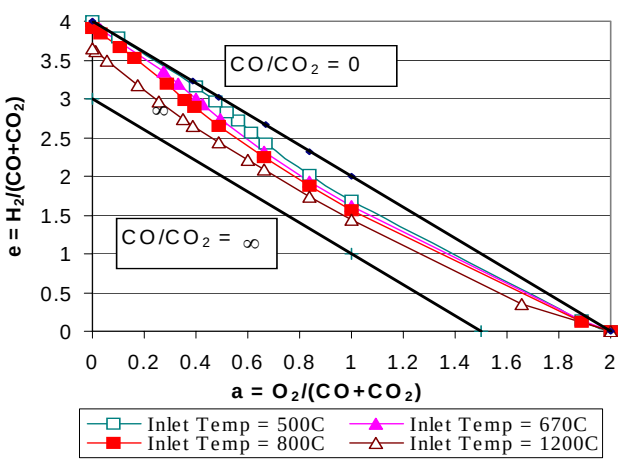

Figure 2. Refrming reaction space for methane at S/C = 6, and P = 97 psig (770 kPa)

ATR Fuel Comparison

Figures 3, 4 and 5 show the reaction space and the effect of inlet temperature on H_2 yield for autothermal reforming of a number of fuels at S/C=3. In these plots of SR versus Hydrogen Ratio (HR), the equilateral triangle bounded by HR = 0, SR = 0 and Equation (3) constitutes the ATR reaction space in the full range of combustion to steam reforming for any fuel. HR is defined as the ratio of the moles of H_2 produced per moles of fuel reformed to (y/2+2x-z). HR is a normalized hydrogen yield, where HR = 1 represents the maximum hydrogen yield for reforming of a given fuel. It is important to mention that the ATR reaction space is independent of conversion, S/C, pressure, temperature, heat loss, assumption of equilibrium, or choice of fuel. Figures 3-5 show that higher inlet temperature generally yields more hydrogen with the maximum hydrogen yield shifting to a lower SR at a given S/C. Table 2 summarizes the maximum H_2 yields and provides the reactor inlet and outlet temperatures for the reforming data shown in Figures 3 to 5. These figures show that HR (i.e. normalized hydrogen yield) increases and experiences a maximum with respect to SR for all fuels. The beneficial effects of increasing inlet feed temperature and fuel LHV on the maximum HR are shown in Figures 6 and 7.

Table 2 - Maximum Normalized H_2 Yield for Various Fuels

Fuel	SR	S/C	Pressure psig (kPa)	T in (°C)	T out (°C)	Maximum HR
Methane	0.254	3	5 (136)	500	649	0.639
	0.199	3	5 (136)	670	649	0.675
	0.181	3	5 (136)	800	649	0.698
Propane	0.244	3	5 (136)	500	649	0.638
	0.179	3	5 (136)	670	649	0.680
	0.131	3	5 (136)	800	649	0.707
Isooctane	0.226	3	5 (136)	500	649	0.646
	0.162	3	5 (136)	670	649	0.687
	0.115	3	5 (136)	800	649	0.713
Dodecane	0.217	3	5 (136)	500	649	0.653
	0.165	3	5 (136)	670	677	0.694
	0.112	3	5 (136)	800	677	0.729
Hexadecane	0.207	3	5 (136)	500	649	0.659
	0.142	3	5 (136)	670	649	0.699
	0.116	3	5 (136)	800	663	0.729

Conclusions

The stoichiometric analysis of the autothermal reaction for a generalized fuel is used to determine the reforming reaction space for methane, propane, isooctane, dodecane, and hexadecane, in the full range of steam reforming to combustion. A methodology is shown for normalizing hydrogen yield data to facilitate direct comparison. The hydrogen yield appears to increase with S/C and inlet temperatures for all fuels. The simulation data and conclusions of this paper are applicable to any ATR regardless of size and are independent of feed flowrates.

References

[1] Hagh, B.F. *International Journal of Hydrogen Energy*, **2003**, 28, 1369-1377.

[2] Douvartzides, S.L.; Coutelieris, F.A.; Demin, A.K.; Tsiakaras, P.E. *AIChE Journal*, **2003**, 49, 248-257.

[3] Ming, Q.; Healey, T.; Allen L., Irving, P. *Catalysis Today*, **2002**, 51-64.

[4] Brown, L.F. *International Journal of Hydrogen Energy*, **2001**, 26, 381-397.

[5] Ahmed, S.; Krumpelt, M. *International Journal of Hydrogen Energy*, **2001**, 26, 291-301.

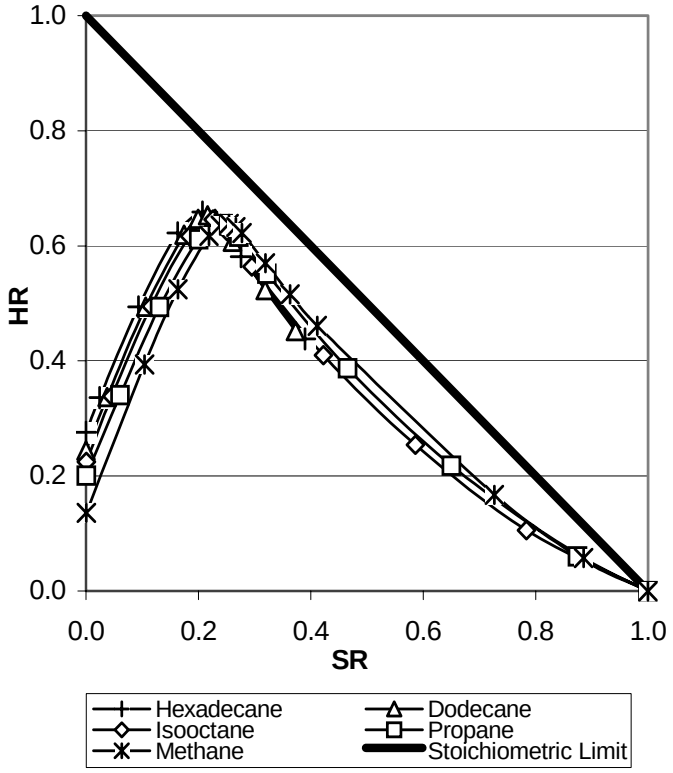

Figure 3. Inlet temperature = 500°C, S/C = 3, P = 5 psig (136 kPa)

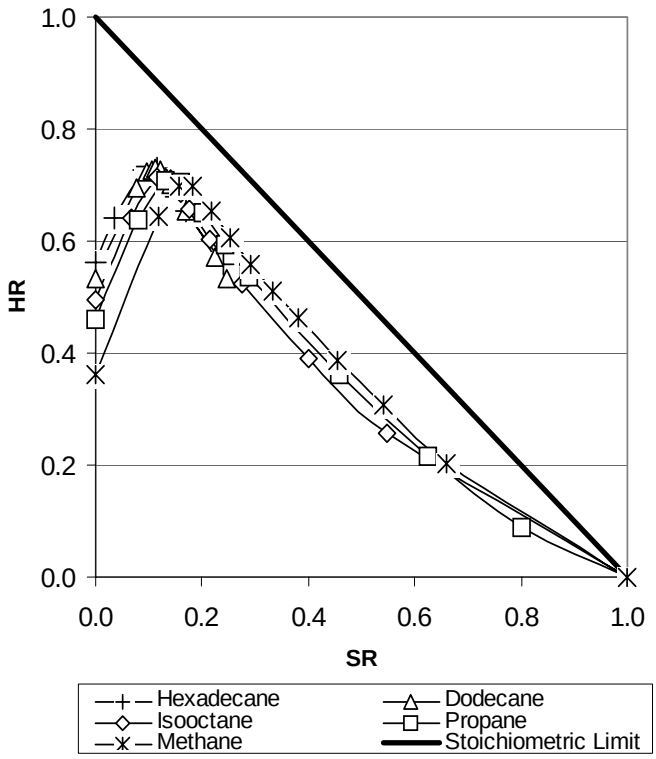

Figure 5. Inlet temperature = 800°C, S/C = 3, P = 5 psig (136 kPa)

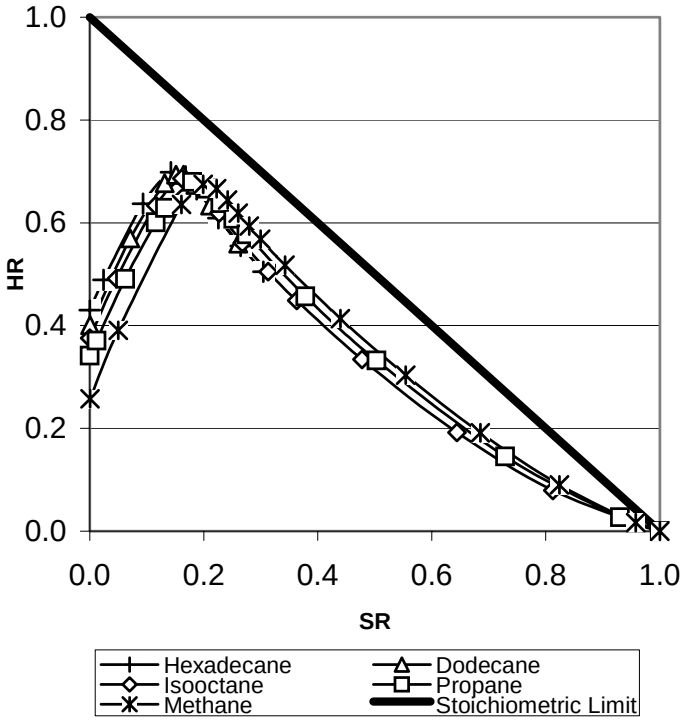

Figure 4. Inlet temperature = 670°C, S/C = 3, P = 5 psig (136 kPa)

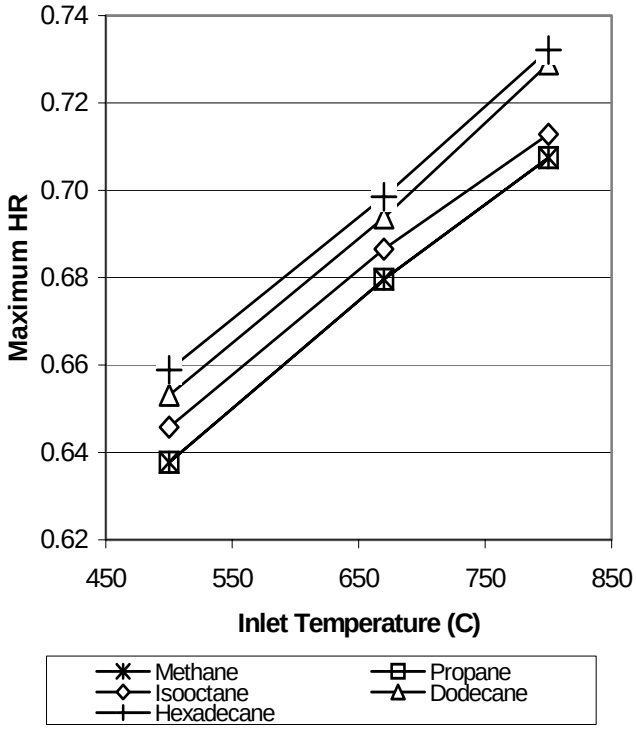

Figure 6. Maximum hydrogen yield at S/C = 3, P = 5 psig (136 kPa)

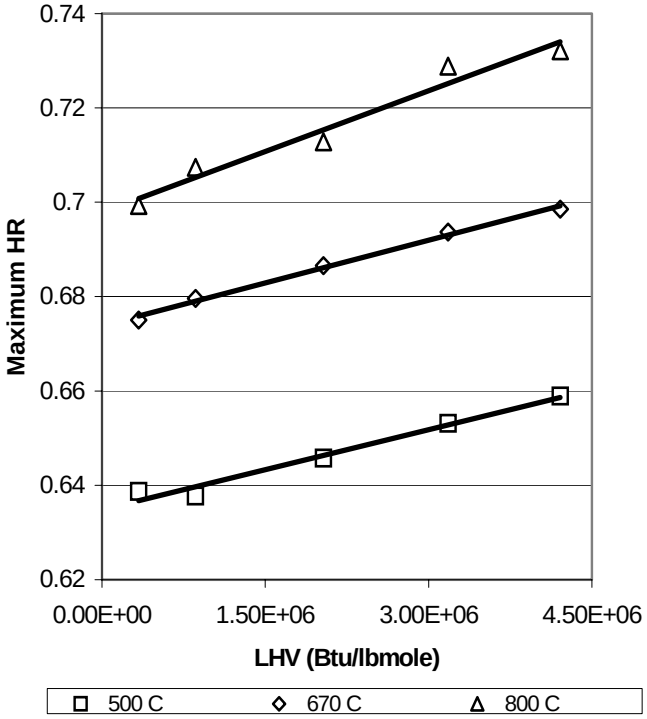

Figure 7. S/C = 3, P = 5 psig (136 kPa)

CATALYTIC REACTOR PERFORMANCE OF A BOROHYDRIDE HYDROGEN GENERATOR

Ying Wu, Qinglin Zhang, Kevin McNamara, Gregory Smith, Joseph Podsiadlik, Ibrahim Qureshi*

Millennium Cell Inc.
1 Industrial Way West, Eatontown, NJ 07724

Introduction

Hydrogen storage is one of the most important issues and potentially the biggest technical barrier to the implementation of a hydrogen economy. Both physical and chemical storage methods are under investigation in order to solve this challenging technical problem. Among all the options, hydrogen storage systems based on chemical hydrides[1,2] have demonstrated gravimetric and volumetric hydrogen storage densities that meet the near term targets and approach the long-term targets of the FreedomCar Initiative. Particularly, sodium borohydride ($NaBH_4$) based systems[3] have shown impressive system performance characteristics.

Sodium Borohydride reacts with water to generate high purity humidified hydrogen gas (H_2) (Eq. 1) suitable for use in proton exchange membrane (PEM) fuel cells. This hydrolysis reaction takes place spontaneously in an un-stabilized solution, and the reaction rate increases dramatically with temperature. Addition of a base such as NaOH or KOH to aqueous solutions of $NaBH_4$ can stabilize the solution against hydrolysis, but the reaction can be initiated again with a suitable catalyst. It is this catalyzed hydrolysis that forms the basis of the Hydrogen on Demand™ (HOD™) technology.

$$NaBH_4 + 4\ H_2O = NaB(OH)_4 + 4\ H_2\uparrow \qquad (1)$$

An effective catalyst is critical to quantitatively and controllably extracting the hydrogen stored in mixtures of borohydride and water. One of the first reports on the catalyzed hydrolysis by Brown[4] examined a number of metals and established relative rates for hydrogen generation using these catalysts. According to Brown, noble metals such as ruthenium (Ru) and rhodium (Rh) are excellent catalysts for this reaction. More recently, less costly metal-boron alloys such as nickel boride and cobalt boride are also reported to be effective catalysts.[5,6]

The desired catalyst has to offer superior reactivity to ensure fast hydrogen generation. High conversion of $NaBH_4$ to H_2 is critical. It is desirable that the catalyst is capable of operating with high concentration $NaBH_4$ fuel over a wide range of fuel throughput (or space velocity). The catalyst also needs to provide fast start-up and be sufficiently durable. Optimization of reactor throughput will result in reduction of catalyst chamber volume and weight, thereby reducing the balance of plant (BOP) in the hydrogen storage system and increase overall gravimetric and volumetric storage efficiencies.

Many factors influence the activity and reactor performance of a catalyst, such as catalyst preparation procedures, catalyst support materials, chemical and morphological transformations of the catalyst surface during reaction, as well as reactor design, operating conditions, and heat and mass transfer issues. To understand the catalyst system, each of these factors should be isolated and studied in detail to the extent possible. In this paper, we report preliminary reactor performance results on a few critical parameters, which include %$NaBH_4$ conversion, liquid feed space velocity, and catalyst durability, of the HOD™ catalysts in a packed bed reactor operating under various hydrogen flow conditions. Results from these studies provide information and direction for further improvements in the catalyst technology.

Experimental

Catalyst Preparation and Fuel Composition The active metal catalyst was supported on a suitable metallic substrate according to methods taught in U.S. Patent 6,534,033 B1[7]. Two catalysts, BMR05 and BMR06, which contain different loadings of active catalyst were selected for detailed evaluation. The fuel solution used in the experiments typically contains 20 wt% $NaBH_4$.

Measurements of Hydrogen Generation Catalyst activity is measured by the apparent hydrogen evolution rates. In many previous reports, hydrogen generation rates were measured from batch type reactors, where a specific amount of catalyst is placed in stagnant or stirring borohydride solution and the resultant hydrogen generation rates measured. In such a configuration, the product sodium metaborate ($NaB(OH)_4$) is mixed with reactant $NaBH_4$ in the same solution, and it is often difficult to achieve close to quantitative conversion of $NaBH_4$ without providing external heating to the solution.

In the results reported below, all hydrogen generation rates were measured using a flow reactor. In a typical experiment, a cylindrical reactor of certain volume is packed with a constant amount of catalyst for testing. One end of the reactor is connected to a fuel line via a metering pump. The rate of liquid flow into the reactor is monitored by the weight change of the fuel reservoir. The other end of the reactor is connected to a liquid-gas separator where hydrogen gas and the liquid by-product, $NaB(OH)_4$ solution, are separated. In the flow reactor, metaborate does not back mix with the $NaBH_4$ reactant solution. The separated hydrogen stream then passes through a condenser and a drying column to remove water and ensure accurate measurement of hydrogen flow rate. Conversion of borohydride to hydrogen, or reaction yield, is calculated by dividing the measured hydrogen flow rate by the theoretical hydrogen flow rate calculated based on the fuel feed rate.

Catalyst Durability Data were collected from semi-continuous operation. The reactor was operated at a constant liquid feed space velocity for 6-8 hours a day. At the end of the day, reactor was shut down and catalyst bed rinsed with water. The next day, same procedures were repeated, and on-stream hours accumulated.

Results and Discussion

Conversion Efficiency and Throughput Sodium borohydride conversion efficiency was measured over a range of fuel flow rates. One of the advantages of borohydride hydrolysis is that the reaction

can go to 100% completion with no side reactions. The challenge in a flow reactor is to maximize the fuel throughput rate while preserving 100% conversion of the reactant. The higher the throughput, the smaller the reactor volume required for a given hydrogen output level. Figure 1 shows typical experimental conversion results. It can be easily seen from the graph that for space velocity up to ~1.25 min^{-1} (or 75 hr^{-1}), conversion of borohydride to hydrogen remains above 95%.

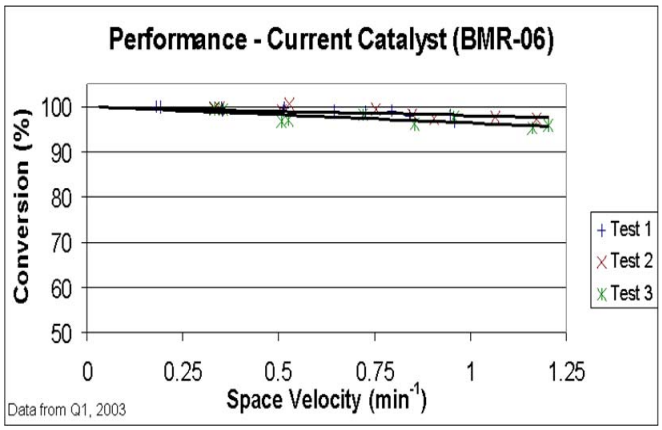

Figure 1. Conversion of $NaBH_4$ at various liquid feed space velocity.

Durability Durability of the catalyst was measured to ensure that there is no drastic deactivation of catalyst. Figure 2 depicts a durability study of catalyst BMR05. Constant performance level was demonstrated for more than 400 hours of run time. Hydrogen generation rate remained relatively constant, about 8.1 SL/min, at a constant liquid fuel feed rate of 18 g/min, corresponding to ~95% $NaBH_4$ conversion throughout the experiment. The three thermocouples evenly spaced along the reactor length recorded steady temperatures between 140-150°C. In a separate durability test

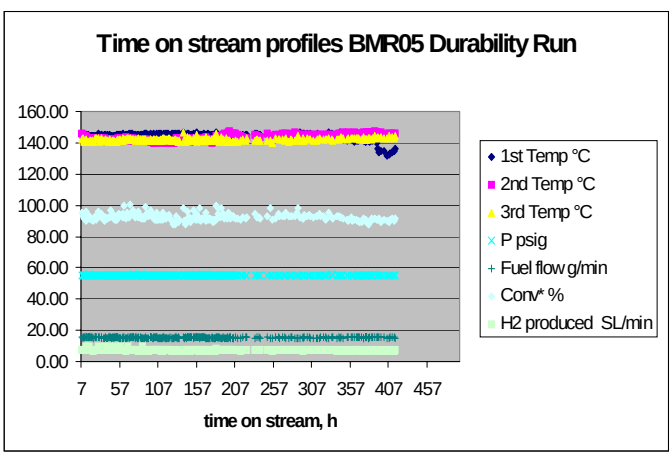

Figure 2. Time on Stream Profile of BMR05. Sodium borohydride conversion, hydrogen flow rate, fuel flow rate, system pressure, and reactor temperatures are plotted as a function of time on stream.

of catalyst BMR06 (based on a slightly modified recipe), more than 700 hours of run time has been accumulated and no significant drop in performance level has been observed. In both experiments, the liquid feed space velocity was maintained at 0.25 min^{-1} (or 15 hr^{-1}), and the system pressure was regulated at 55 psig.

Additional data also indicate that durability of the catalyst varies with different catalyst supports. In some cases, only a few days of high conversion operation was sustained before the catalyst became ineffective. Furthermore, catalyst durability often decreased with increasing liquid feed space velocity. More extended durability studies will be carried out as catalyst preparation procedures and materials properties are optimized. We expect to be able to demonstrate catalyst durability on the order of several thousand hours.

Conclusions

Higher sodium borohydride conversion can be achieved over a wide range of fuel feed space velocity in a packed bed flow reactor system. The reaction is self-sustaining, without need for external heating to achieve higher % conversion. Initial durability studies indicated that the current generation of catalyst can be operated for more than 700 hours on stream without significant loss in activity. Further improvements can be made on durability by optimizing catalyst preparation procedures and reactor engineering.

Overall optimization of the catalyst will depend on our increased understanding of the catalyst composition, structure, as well as reactor operation conditions.

References

(1) Bogdanovic, B.; Schwickardi, M. *J. Alloys Compounds* **1997**, 1-9.

(2) Schlapbach, L.; Zuttel, A. *Nature* **2001**, 353-358.

(3) Mohring, R. M.; Eason, I. A.; Fennimore, K. A. *SAE Technical Paper # 2002-01-0098* **2002**.

(4) Brown, M. C. *Journal of American Chemical Society* **1962**, *84*, 1493-1495.

(5) Holbrook, K. A.; Twist, P. J. *J. Chem. Soc. (A)* **1971**, *1971*, 890-894.

(6) Dong, H.; Yang, H.; Ai, X.; Cha, C. *International Journal of Hydrogen Energy* **2003**, 1095-1100.

(7) Amendola, S.; Binder, M.; Sharp-Goldman, S.; Kelly, M.; Petillo, P.; Millennium Cell Inc.: USA, 2003.

CHEMICAL HYDROGEN STORAGE IN NANO-STRUCTURED MATERIALS. CONTROL OF HYDROGEN RELEASE AND REACTIVITY FROM AMMONIA BORANE COMPLEXES.

Tom Autrey, Anna Gutowska, Liyu Li, John Linehan, Maciej Gutowski

Pacific Northwest National Laboratory, Richland, WA 99352, USA

Introduction

The DOE has recently issued a Grand Challenge in Hydrogen Storage to compliment existing programs on Hydrogen Production and Fuel Cell development.[1] In response to this challenge we have initiated a program that uses a combination of experimental and computational approaches to investigate the potential of NH_xBH_x (x=1-4) as chemical hydrogen storage materials for on-board hydrogen storage. Our initial computational results suggest that the step-wise process is not greatly exothermic.[2] If true, these materials may provide great hope for a reversible hydrogen storage material with high volumetric and gravimetric density for on-board storage.[3] The optimum thermal decomposition reaction $NH_4BH_4 \rightarrow BN + 4H_2$, occurs by a four-step process and provides a theoretical yield of 24 wt% hydrogen far exceeding DOE's most ambitious goals. Even if two of the four steps prove feasible H_2 capacities of greater than 12 weight % would be realized. In this present work we have focused our experimental efforts on ammonia-borane [NH_3BH_3]. In the solid state ammonia-borane (AB) undergoes a rapid dehydropolymerization reaction upon melting at 115 ˚C to yield polyammonia-borane [$(NH_2BH_2)_n$], an inorganic analog of polyethylene, + H_2.[4] In a subsequent step the $(NH_2BH_2)_n$ decomposes to [$(NHBH)_2$], an inorganic analog of polyacetylene, + H_2 at 170 ˚C.[5] An undesirable side reaction, formation of the cyclic borazine $(NHBH)_3$, an inorganic analog of benzene, has also been observed to form from the bulk material at the higher temperatures. Borazine is an undesirable side product due to its high vapor pressure. Given the stringent requirements of hydrogen purity for fuel cell applications it will be important to minimize side reactions. One of the major goals of this work was to use the nanometer diameter pores of mesoporous templates to control the selectivity of the hydrogen release pathways from ammonia-borane and polyammonia-borane.

Experimental

Ammonia borane was purchased from Aldrich (90% tech) and purified by recrystallization from diethyl ether followed by a wash with ethanol to remove polymeric and borate impurities to yield >99% pure NH_3BH_3 by ^{11}B NMR. Analyses were performed using a Netzsch STA 409 TGA/DSC and a Pfeiffer QMS300 MS or a Setaram C80 Calorimeter. In the Netzsch equipment a heated fused silica capillary (200 ˚C) was used to transfer the off gas from the TGA to the MS. The MS uses a standard electron impact ionization detector. The MS scanning rate was 12 seconds for a range of 1 to 100 amu. A thermal ramp of 5 ˚C/min from room temperature to 250 ˚C using an argon flow of 100 cc/min was used in our analysis.

Results and Discussion

Preparation of mesoporous templated ammonia-borane. Mesoporous silica templates have extremely high surface area and a highly ordered pore structure by virtue of surfactant templated synthetic process.[6] The material used in this work, SBA-15, prepared according to literature procedures for another project, was characterized and found to have average particle 100-200 μm, surface area 1000 m^2/g, pore diameter 3 nm. A sample of 50 mg of the SBA-15 was exposed to a 300 μL methanolic solution containing 50 mg of AB. Given the porous nature of the material we expected capillary action to fill the internal channels of the mesoporous template. The 'wet' SBA-15 was dried under vacuum to produce a sample with an internal coating of ammonia-borane (ca. 1:1 wt% AB to SBA-15). Comparison of SEM images of the material before and after coating with AB showed very similar features as shown in Figure 1. We expected to visually observe clumping of the solid AB on the template if we were not successful in our attempt to coat the internal channels. An EDM scan of the 1:1 mixture of AB:SBA-15 sample also produced very little signal from N and B and we again would have expected a greater signal if the AB was not efficiently deposited within the core structures of the SBA-15. Given these negative observations we assumed that we had a sample of SBA-15 mesoporous template with internal pores coated with monomeric ammonia-borane.

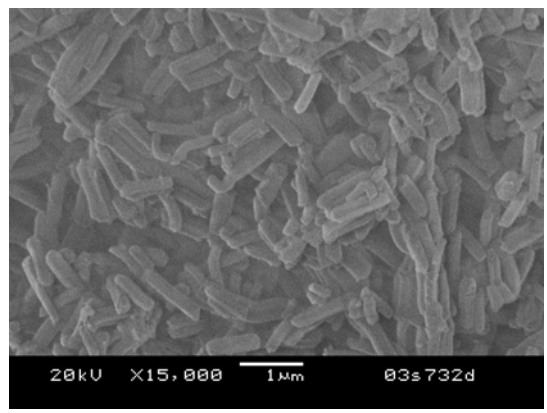

Figure 1. SEM image of 1:1 Mixture of AB:SBA-15. We could observe no difference in the image before or after AB was added. The EDM scan showed no evidence for either Boron or Nitrogen. These observations lead us to assume that the AB was deposited as a thin layer within the mesoporous template.

Calorimetric and mass spectroscopy studies of ammonia-borane , thermolysis in mesoporous silica templates. In order to test our hypothesis that the yield of borazine [*c*-$(NHBH)_3$], an inorganic analog of benzene, would be reduced when the AB was heated as a 1:1 weight mixture, we undertook differential scanning calorimetry (DSC) experiments to compare the neat bulk material to our 1:1 AB:SBA-15 sample prepared as described above. It is likely that hydrogen formation occurs by an intermolecular dimerization pathway as shown in equation 1,[7] however a two-step mechanism can not be completely ruled out, eqs 2 and 3.

(1) $2\ NH_3BH_3 \rightarrow NH_3BH_2\text{-}NH_2BH_3 + H_2$

(2) $NH_3BH_3 \rightarrow NH_2{=}BH_2 + 2H_2$

(3) $2NH_2{=}BH_2 \rightarrow NH_3BH_2\text{-}NH_2BH_3$

If reaction 1 is the mechanistic pathway then it follows that the dimer would form oligomers through subsequent bimolecular dehydopolymerization pathways. Each step that forms a new B-N bond also forms hydrogen, eqs 4 and 5.

(4) $NH_3BH_3 + NH_3BH_2\text{-}NH_2BH_3$
$\rightarrow NH_3BH_2\text{-}NH_2BH_2\text{-}NH_2BH_3 + H_2$
(5) $NH_3BH_3 + NH_3BH_2NH_2BH_2\text{-}NH_2BH_3$
$\rightarrow NH_3BH_2\text{-}NH_2BH_2\text{-}NH_2BH_2\text{-}NH_2BH_3 + H_2$

As the temperature approaches 170 ˚C additional hydrogen is released, eqs, 6 and 7. However, a competing side reaction is cyclization to form borazine, eq 8.[8]

(6) $(NH_3BH_2NH_2BH_2\text{-}NH_2BH_3)_n$
$\rightarrow (NH_3BH_2NH_2BH{=}NHBH_3)_n + H_2$
(7) $(NH_3BH_2NH_2BH{=}NHBH_3)_n$
$\rightarrow (NH_3BH{=}NHBH{=}NHBH_3)_n + H_2$
(8) $(NH_3BH{=}NHBH{=}NHBH_3)_n \rightarrow$ borazine + H_2

Under optimum conditions we want to minimize cyclization, reaction (8) and optimize further dehydrogentation, i.e., reactions (6 and 7). We expected that if the AB was coated on the inside of the mesoporous silica template that the template would minimize borazine formation by controlling linear polymer growth and minimizing cyclization. To test this hypothesis DSC experiments were preformed with both the neat AB and the 1:1 mixture of AB:SBA-15. Two results are notable. First, as hoped, borazine formation appears to have been substantially reduced when AB is heated as the 1:1 composite with SBA-15. It is below the detection limits of our mass detector. Even when the flow rate of argon is reduced to 40 cc/minute we did not detect borazine, though hydrogen release was still observed at ca. 170 ˚C, temperature corresponding to borazine formation in the neat AB. Second, a surprising result, the observation that hydrogen is released in the initial step, eq 1, at a significantly lower temperature when the AB is heated as the 1:1 composite with SBA-15! This result is illustrated in Figures 2. This novel finding is especially attractive given that a

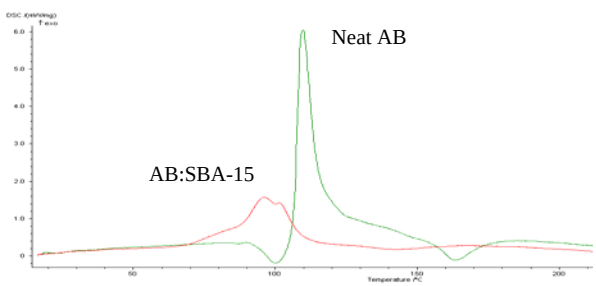

Figure 2. Comparison of DSC scan (temperature vs power) of neat AB (green line) and 1:1 AB:SBA-15 mixture (red line). Ramp rate 5 ˚C/min from room temperature to 250 ˚C. The peak of the exotherm is 110 ˚C for neat AB and 96 ˚C for the mixture.

fundamental requirement for on-board storage is the release of H_2 at temperatures below 100 ˚C. In the 1:1 AB:SBA-15 sample hydrogen is released at 96 ˚C compared to the 110 ˚C for the neat AB sample.

Conclusions

In this paper we present the results of our efforts using the mesoporous silicate template (SBA-15) to control the chemistry of dehydropolymerization of ammonia-borane (AB) to yield gaseous hydrogen. Thermolysis of AB in the SBA-15 template shows two profound effects different than observed in the bulk thermal reaction: (i) hydrogen is released from AB at significantly lower temperatures (well below 100 ˚C) and (ii) contrary to observations that borazine is formed in bulk AB thermolysis, no borazine is detected in AB thermolysis in the mesoporous template.

Acknowledgement. This research was performed in part using the Interfacial and Nano Science facility in the William R. Wiley Environmental Molecular Sciences Laboratory, a national scientific user facility sponsored by the U.S. Department of Energy's Office of Biological and Environmental Research and located at the Pacific Northwest National Laboratory. Pacific Northwest is operated for the Department of Energy by Battelle. The authors wish to acknowledge support from the Laboratory Directed Research and Development Program at the PNNL and the Nano Science and Technology Initiative and Dr. Yongsoon Shin for providing us with the SBA-15 and Jim Coleman for the SEM images. TA wishes to thank T Baker (LANL), L Sneddon (U Penn) and M Heinekey (U Washington) for very informative discussions on AB chemistry.

References

(1) Hydrogen, Fuel Cells & Infrastructure Technologies Program, 2003 Merit Review and Peer Evaluation Meeting, May 19-22, Berkeley, CA.
(2) See Fuel Prints this issue Symposium on Molecular Modeling and Reaction Chemistry. M. Gutowski and T. Autrey, *Prepr. Pap. –Am. Chem. Soc., Div. Fuel Chem.* **2004**, 49(2) xxxx.
(3) It has recently been shown that conversion of ammonia-borane to polyaminoborane is exothermic by less than 7 kcal/mol. G. Wolf, J. Baumann, F. Baitalow, F.P. Hoffman, *Thermochim. Acta* **2000**, *343*, 19.
(4) V. Sit, R.A. Geanangel, W.W. Wendlandt *Thermochim. Acta* **1987**, *113*, 379.
(5) F. Baitalow, J. Bauman, G. Wolf, K. Jaenicke-Röβler, G. Leitner *Thermochim. Acta* **2002**, *391*, 159.
(6) Zhao, D., Feng, J., Huo, Q., Melosh, N., Fredrickson, G. H., Chmelka, B. F., Stucky, G. D. *Science* **1998**, *279*, 548.
(7) C. A. Jaska; K Temple; A. J. Lough; I. Manners. *J. Am. Chem. Soc*. **2003**, *125*, 9424.
(8) T. Wideman, L.G. Sneddon *Inorg. Chem.* **1995**, *34*, 1002.

THEORETICAL PERSPECTIVE ON IMPROVING KINETICS IN Mg HYDROGEN STORAGE

Jian-jie Liang, Nazy Khosrovani

Accelrys Inc.
9685 Scranton Rd
San Diego, Ca 92121

Introduction

Magnesium, forming ionic, transparent MgH_2 containing 7.6 mass% hydrogen, is among those that are most-promising in hydrogen-storage materials for mobile applications [1]. However, the formation from bulk Mg and gaseous hydrogen is not only extremely slow, but requires elevated temperatures (300 °C at 1 bar pressure) as well, with the reverse process requiring similar conditions [2]. Numerous factors can contribute to the kinetics of the forward and reverse reactions in the hydrogen storage processes [3]. Among them, molecular hydrogen dissociation and hydrogen diffusion are two factors of primary concern. It's already known that hydrogen diffuses only extremely slowly in crystalline Mg, with a diffusion constant in the order of 10^{-16} cm^2/s [4]. This translates to that the mean time ($d^2/6D$, where D is the diffusion constant) for hydrogen to diffuse through a 1 μm Mg particle will be in the order of 10^3 S. One may hope that reducing the particle sizes to nanometers will speed up the kinetics, only to see no significant improvement [5]. It therefore appears that molecular hydrogen dissociation on Mg surfaces is a rate-limiting process.

It had been demonstrated recently [6] that Density Functional Theories (DFT) approach can be used to successfully explore tailoring the energetics of Mg hydrogen sorption/desorption processes, fundamentals that are responsible for properties such as diffusion rate and nucleation. The same principles should apply in exploring aspects in the hydrogen dissociation process, as shown in the literature [7, 8]. In the present work, DFT method was used to look at hydrogen dissociation on both unmodified- and transition metal modified-Mg 100 surface. Energy barrier, surface sorption energy, and surface diffusion barrier are the main focuses of the work.

Method

$Dmol^3$ [9], a Density Functional Theory (DFT) method available in the software package, Materials Studio, was used in the calculations. The setup parameters were similar to those used previously in the thermochemical studies of similar materials [6].

Experimental structure of Mg [10] was used as starting model to obtain the DFT relaxed structure that was identical to what was found in previous study [6]. The 100 surface (Fig. 1A) was constructed based on the DFT optimized bulk structure. Surface suppercell of 4 x 2 was built such that the calculated hydrogen dissociation barrier (see later sections) becomes invariant as a function of cell size, with respect to a set of k-point density. To model the surface environment, a vacuum space of 20 Å was added on top of the surface such that 3D periodic conditions can be used in the summation of the energy terms in the DFT calculations. A total of 4 Mg layers (corresponding to 4-unit cell depth perpendicular to the 100 surface) were used in the calculations. Mg atoms in the surface layer and the layer immediately beneath were allowed to relax prior to introducing hydrogen into the systems. In most cases, one of the surface Mg atoms would be replaced by a transition mental atom (e.g., Fe as in Fig. 1D), and the surface structure reoptimized.

For unmodified Mg 100 surface, two hydrogen dissociation geometries were considered (Fig. 1B&C), corresponding to the hydrogen molecule approaching the surface towards the center of gravity ("atop") of a single Mg atom and towards the "bridge" between two Mg atoms, respectively, and dissociate into the nearby hollows surrounded by 3 Mg atoms. For transition metal-doped surfaces, only the atop configuration was considered, as the bridge configurations were not stable in these circumstances and evolved into atop configuration eventually. A single hydrogen molecule was placed in the middle of the vacuum space (~ 10 Å above the surface) for the initial configuration of the dissociation process.

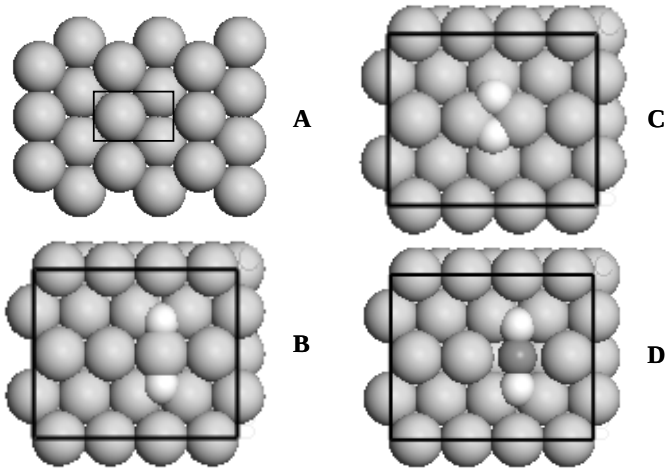

Figure 1. Mg 100 surface used in the calculations. A. the surface layer (1-unit cell depth). The rectangle outlines the original surface unit cell; B. actual simulation cell (4 x 2 x 4) with the adsorbed hydrogens through the "atop" configuration; C. same as B, but with the adsorbed hydrogens through the "bridge" configuration; D. same as B, but with a transition metal (here Fe) atom replacing Mg. Large grey ball: Mg; small, light grey ball: H; small, dark grey ball: Fe.

Transition state search engine available in the Dmol3 package was used for all transition state calculations. Full LST/QST [11] search were performed on each and every sample system, and usually followed by a transition state optimization calculation.

When transition state search failed to produce a transition state (usually associated with transition metal-doped surfaces), the approach of potential energy surface (PES) was used to confirm the nature of unactivated dissociations of hydrogen on such surfaces.

Results and Discussions

The calculated energy barriers, along with the energetic and structural parameters of the corresponding transition states (if exist) are given in Table 1. Note here the enthalpy of reaction (ΔH_f) refers to the difference directly between the total energy of the state when the hydrogen molecule is in the middle of the vacuum space (~ 10 Å above the surface) and that when hydrogen is dissociated into the hollows (state obtained through geometry optimization).

Dissociations on unmodified Mg 100 surface. Hydrogen Dissociations are activated in either atop or bridge configuration (Table 1), with dissociation barriers of ~ 92 kJ/mol. This is in qualitative agreement with earlier theoretical and experimental studies [8, 12] on a different surface (Mg 0001). It's important to note that the enthalpies of reaction are very small (slightly exothermic in atop configuration and slightly endothermic in the bridge configuration) compared to the energy barrier (Fig. 2). In other words, the activation

barrier is the factor that controls the rate of both forward (sorption) and reverse (desorption) processes, and the barrier height dictates the temperature and pressure conditions of both the sorption and desorption processes.

Table 1. Thermodynamic and structural data of H_2 dissociation/absorption on Mg 100 surface

Surface dopent	Ea (kJ/mol)	ΔH_f (kJ/mol)	Ed (kJ/mol)	d_{H-H} (Å)
Unmodified				
atop	91.92	-1.92	minimal	1.28
bridge	92.42	14.52	minimal	1.12
V	51.80	-111.13		1.14
Pd	60.79	-3.56	20.46	1.39
Cu	64.64	-15.86	22.47	1.29
Ni	17.28	-63.85	45.23	1.20
Fe		-100.75	52.05	
Co		-90.04	59.08	
Ti		-105.56	56.44	

Ea: activation energy
ΔH_f: enthalpy of reaction (surface sorption)
Ed: surface diffusion barrier, corresponding to hydrogen diffusion from a hollow with the transition metal being one of the 3 coordinating atoms to a nearby hollow
d_{H-H}: H – H distance at transition state

Dissociation on transition metal-doped surfaces. Most experimental and theoretical studies on the interaction of hydrogen with metal surfaces today involve elemental d-transition metal surfaces; some concern transition alloy surfaces [3]. However, due to the intrinsically low weight percentage of absorbed hydrogen in pure transition metals, and the problem of alloy degradation after repeated cycling of hydrogen sorption and desorption, it becomes increasingly urgent for new thinking in materials design, probably based on the known potential hydrogen storage materials.

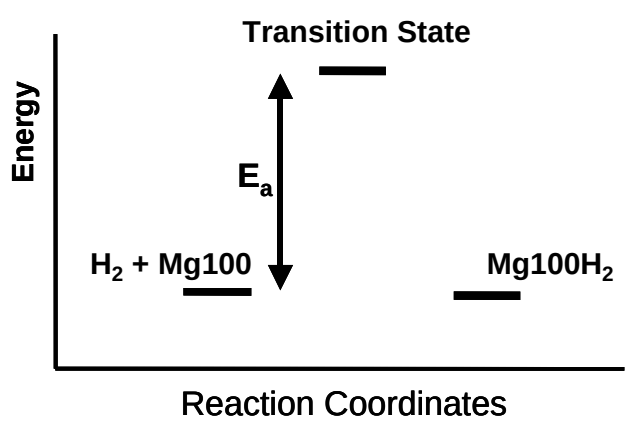

Figure 2. Activated dissociation (with energy barrier, Ea) of hydrogen on Mg 100 surface through the "atop" configuration. Note there is only a minimal difference in system energy (1.92 kJ/mol) between the starting materials (H_2 + Mg 100) and the final product (Mg 100 H_2).

Surface doping on Mg nanoparticles may offer a solution to the dilemma – transition metals doped on the particle surface may accelerate the dissociation of the hydrogen molecules, and particle size in nano-scales will make a very slow diffusion of hydrogen in, e.g., Mg particles to complete in an acceptable time scale.

It can be seen from Table 1 that activation barriers can indeed be lowered substantially, some even become unactivated (when doped with Fe, Co, or Ti). It is interesting to recognize that hydrogen dissociation over a transition metal (when doped on to the Mg 100 surface) may behave differently as appose to that on the corresponding bulk transition metal surface. For example, dissociation over Pd metal surface had been shown both experimentally and theoretically to be unactivated [13, 14, 15]. However, when doped on to the Mg 100 surface, the dissociation on the Pd atom will be activated, with a barrier of ~ 61 kJ/mol (Table 1).

Among the 7 (Table 1) commonly considered transition metals in hydrogen storage applications, 3 (Fe, Co, Ti) show unactivated dissociation when hydrogen molecule approaches the transition metal doped on to the Mg 100 surface. However, notice the associated exothermic enthalpies of reaction between 90 and 106 kJ/mol, which are in the same order of magnitude as that of the energy barrier of hydrogen dissociation over unmodified Mg 100 surface (Fig. 3). That means, while unactivated in the forward (sorption) process, it'll take similar pressure and temperature conditions for the reverse (desorption) process as for pure Mg. It is also important to notice the relatively high diffusion barrier (note there is essentially no surface diffusion barrier on unmodified Mg 100 surface), signifying potentially added difficulty diffusing into the Mg lattice beneath.

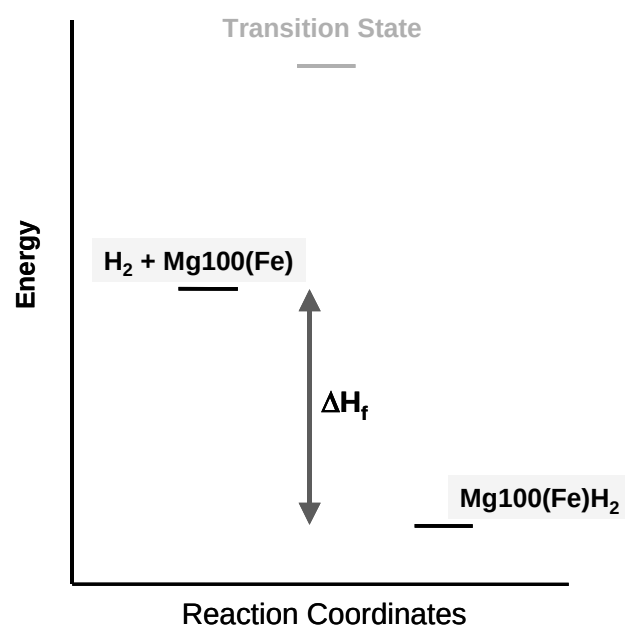

Figure 3. Unactivated dissociation of hydrogen on Fe-doped Mg 100 surface through the "atop" configuration (centered on the Fe atom. Refer to Fig. 1D). The energy barrier (the water-marked "Transition State") of the activated dissociation on unmodified Mg 100 surface was shown as a reference. ΔH_f: enthalpy of formation of the reaction.

Among the 4 doping transition metals (V, Pd, Cu, Ni) that are associated with activated dissociation, although giving a low activation barrier of ~ 17 kJ/mol, Ni is associated with a rather high enthalpy of reaction of ~ 64 kJ/mol. The combined energy needed for the reverse (desorption) process is 81 (17 + 64) kJ/mol, which approaches the barrier associated with unmodified Mg 100 surface. That probably explains why, while the hydrogen sorption process of the Mg2Ni alloy is relatively rapid, the desorption process was found to remain sluggish [1]; Vanadium presented a rather undesirable combination of relatively high activation barrier and the enthalpy of reaction, and was not considered further; Pd and Cu offer a reduction of ~ 30 kJ/mol in activation energy, and relatively low enthalpies of reaction, together with low surface diffusion barriers. In particular, Pd is associated with a minimal enthalpy of reaction (~ 3 kJ/mol), making reduced pressure and temperature conditions possible for both sorption and desorption processes.

Conclusions

Hydrogen dissociations on unmodified Mg 100 surface were found to be activated, with barriers around 92 kJ/mol. When doped with transition metals, the dissociation barrier can be lowered, in some cases to the extent of being unactivated. Pd doping was found to be the most promising, based on the considerations of the activation barrier, energy requirement for reverse (desorption) process, and surface diffusion barrier.

Acknowledgement: We thank Niri Govind, Accelrys Inc., for providing preprint on the publication on the LST/QST method. We also thank the HP Company for the computing resources.

References

1. L. Schlapbach and A. Zuttel, Nature **414**, 353 (2001)
2. L. Schlapbach (e.d.) Hydrogen in Intermetallic Compounds I. Electronic, Thermodynamic, and Crystallographyic Properties (Topics in Applied Physics Vol 63) (Springer, 1988)
3. L. Schlapbach (e.d.) Hydrogen in Intermetallic Compounds II. Surface and Dynamic Properties, Applications (Topics in Applied Physics Vol 67) (Springer, 1992)
4. P. Spatz, H. A. Aebischer, A. Krozer, and L. Schlapbach, Z. Phys. Checm. 181 (1993) p. 393
5. S. Orimo and H. Fujii, Appl. Phys. **A** 72 (2001) p. 167
6. J. Liang, Appl. Phys. **A** (2003) in press
7. J. Harris: Appl. Phys. **A** 47 (1988) p. 63
8. D. M. Bird, L. J. Clarke, M. C. Payne, I. Stich, Chem. Phys. Lett. 212 (1993) 518
9. B. Delley, J. Chem. Phys. **92**, 508 (1990)
10. R.W.G. Wyckoff, in *Crystal Structures*, volume 1 (Interscience, John Wiley & Sons, 1963).
11. N. Govind, M. Petersen, G. Fitzgerald, D. King-Smith, J. Andzelm, Computational Materials Science (2003), in press
12. R. B. Murphy, J. M. Mundnar, K. D. Tsuei, E. W. Plummer: Bull. Am. Phys. Soc. **33**, 655 (1988)
13. K. D. Rendulic, G. Anger and A. Winkler, Surf. Sci. 208 (1989) 404
14. A. Gross, S. Wilke, and M. Scheffler, Phy. Rev. Lett. 75 (1995) 2718
15. A. Eichler, J. Hafner, A. Grob, and M. Scheffler, Phys. Rev. B 59 (1999) 13297

NANOCRYSTALLINE GOLD CERIA-BASED WATER –GAS SHIFT CATALYSTS FOR FUEL CELL APPILICATIONS

Ivan C. Lee and Deryn Chu

AMSRD-ARL-SE-DC
US Army Research Laboratory
2800 Powder Mill Road
Adelphi, MD 20904

Abstract

New gold/ceria-based water-gas shift (WGS) catalysts have been developed to clean up carbon monoxide in hydrogen-rich gas for fuel cell applications. The new water-gas shift catalyst, $Au/MgO/Ce_{0.8}Sm_{0.15}Gd_{0.05}O_{1.9}$, is non-pyrophoric and has high WGS activities at low temperature (below 300 ^oC) with $H_2/CO=1$ in the feed. This nanocystalline(<10nm) $Au/MgO/Ce_{0.8}Sm_{0.15}Gd_{0.05}O_{1.9}$ catalyst was synthesized by carbonate co-precipitation of doped ceria followed by gold deposition with urea. The durability of Sm- and Gd-doped ceria as low-temperature water-gas shift (WGS) catalysts was tested with argon gas saturated with water at elevated catalyst temperatures. The SEM and BET surface area analysis indicated that there were no significant changes at 350°C for 10 hours. We have evaluated the WGS activities of various ceria-based catalysts containing Au, Sm, Gd, Zr and Mg at CO/H2= 1. Our results indicate that the presence of Au and MgO in $Au/MgO/Ce_{0.8}Sm_{0.15}Gd_{0.05}O_{1.9}$ plays significant roles in the WGS reaction. No methane is produced in our studies.

Introduction

An integrated system of a fuel reformer and a fuel cell can provide portable and mobile power for battery chargers and scout vehicle silent watch. Diesel fuel reformers produce hydrogen for fuel cells[1,2]. Unfortunately, the diesel fuel reformers also produce appreciable amount of CO. For instance, catalytic partial oxidation gives ~ 48 % CO (N_2-free and dry basis)[1], while steam reforming produces 16% CO (dry basis)[2]. Since the tolerable level of carbon monoxide in PEM fuel cells is about 10 ppm, one or several intermediate carbon monoxide cleanup steps (such as water-gas shift reactor) are necessary.

The primary objective is to develop a novel low temperature water-gas shift catalyst to clean up carbon monoxide in the hydrogen-rich reformate. The water-gas shift (WGS) reaction ($CO + H_2O \rightleftharpoons CO_2 + H_2$) currently attracts lots of attention because the deactivation of commercial $Cu/ZnO/Al_2O_3$ water-gas shift catalysts is a major technical barrier for fuel processors. Gold/ceria-based catalysts can potentially replace the copper-based catalysts for water-gas shift reaction[3-7]. However, there have been some controversies on the reducibility of ceria[8] and the deactivation of gold/ceria materials[9].

This paper summarizes our recent research efforts to develop metal/doped-ceria as low-temperature WGS catalysts. Our approach for water gas shift catalyst development is to prepare nanocrystalline ceria-based catalysts, and then measure the catalyst activity with realistic reformate compositions (H_2/CO ratio =1). Oxides of Mg, Zr, as well as lanthanides, such as Ce, Sm and Gd, have been chosen as support materials in this study.

Experimental

Material Synthesis. The synthesis of gold catalyst was a two-step process. First, nanocrystalline supports made of ceria doped with samarium and gadolinium were prepared by carbonate co-precipitation. Next, gold nanocrystallites were deposited onto doped ceria support materials by deposition-precipitation with urea.

Doped ceria support materials were produced via co-precipitation using ammonium carbonate and solutions of 0.15 M $Ce(NO_3)_3$, $Sm(NO_3)_3$ and $Gd(NO_3)_3$. Typically, 80 cm^3 of $Ce(NO_3)_3$, 15 cm^3 of $Sm(NO_3)_3$ and 5 cm^3 of $Gd(NO_3)_3$ were added into 100 cm^3 of 1.5 M ammonium carbonate solution. The mixture was stirred continuously and was controlled at 65°C by a circulated water bath. The resultant suspension was homogenized and then filtered under vacuum. The precipitate was washed with de-ionized water and then with ethanol. The precipitate was allowed to dry overnight. Finally, it was crushed and was calcined in a tube furnace under flowing O_2 (150 cc/min) at 600°C. The ramping and cooling rates of the furnace were controlled at 5°C/min. The calcination temperature of 600°C was chosen based on our thermogravimetric analysis (TGA) with a Perkin Elmer TGA7 analyzer.

Characterization. X-ray diffraction (XRD) measurements were performed using a Philips PW 1840 diffractometer operated at 40 kV/20 mA. Line broadening analysis of <220> and <111> planes determined the crystallite sizes of doped ceria and gold, respectively.

Multi-point BET surface areas of the water-gas shift materials were determined with a Micromeritics ASAP 2010 Automatic Physisorption Analyzer. The samples were degassed at 250°C, and the sample tubes were backfilled with nitrogen. Then 11 equilibrium data points of nitrogen adsorption were taken at relative pressures between 0.05 and 0.3.

The material morphology and elemental composition analysis were performed with a Hitachi S4500 field-emission scanning electron microscope (SEM) equipped with an energy dispersive X-ray spectrometer (EDX). The sample morphology was further examined with a JEOL 2010 transmission electron microscope (TEM) operated at 200 kV. High resolution images show lattice fringes and allow the examination of particle size and crystalline structure. The sample powder was suspended in ethanol using a ultrasonic bath and was deposited on a 400-mesh Cu grid.

Durability and Activity Tests. The durability of the gold catalyst was tested by flowing humidified argon at an elevated temperature. 75.0 sccm of argon was saturated with H_2O with a gas bubbler at 76.2^{o}C. This corresponds to about 50 sccm of water vapor. This humidified argon stream was fed into a quartz tube with 0.2 g of supported gold catalyst in a tube furnace at 350°C for 3 or 10 hours. Then the catalysts were analyzed with SEM, TEM and BET surface area measurements.

We measured the reaction rates for WGS at atmospheric pressure with powder catalysts loaded at the center of a ¼"tubular quartz reactor. All catalysts were non-pyrophoric, and they were used as prepared without activation. We injected the water into the flowing gas stream by a HPLC liquid pump and vaporized in the heated gas line before entering the reactor. The water in the reactor exit stream was collected by an ice-water condenser. The product gas stream was then analyzed on line simultaneously by two columns of an Agilent 3000 micro-gas chromatograph. A molecular sieve column (using argon as carrier gas) separates the carbon monoxide, hydrogen and methane; the Plot U column (using helium as carrier gas) separates the carbon dioxide. Then the reaction rate was calculated by the carbon dioxide product, and the rate was normalized by the weight of catalyst.

Results and Discussion

Tables 1 and 2 illustrate some characterization results of the water-gas shift materials developed in this work. Our results indicate that we can produce ceria particles of less than 10 nm by carbonate (co)precipitation (Table 1). For comparison, we also synthesized ceria by thermal deposition of solid cerium nitrate hexahydrate [$Ce(NO_3)_3*6H_2O$]. We used TGA to determine the optimum calcination temperatures of all ceria materials from their precursors. The optimum calcinations temperatures were chosen based on our TGA profiles and the subsequent XRD diffraction patterns so that ceria was produced in a fluorite crystal structure.

Table 1. Characterization of Pure Ceria, $\phi = 6/(S\rho)$; Density of Pure Ceria, $\rho = 7.184$ g/cm^3

Method	Surface Area (S), m^2/g	Spherical Diameter (ϕ), nm
Thermal Decomposition	57	14.8
Carbonate (Co)Precipitation	129	6.47
Flame Synthesis	154 [10]	5.44

The XRD and BET analysis (Table 2) show that thermal decomposition (Sample II) produces ceria with larger crystallites and a smaller surface area than carbonate precipitation (Sample I). Table 2 also indicates that doping ceria with 20% of other lanthanides, such as Sm and Gd (Samples III-V), would increase the crystallite size and would decrease the surface area. The reaction temperatures of Samples IV and V are different during co-precipitation. Higher reaction temperature in Sample V increased the surface area of the doped ceria. Supported gold catalysts (Sample VI) were prepared using Sample V as the support materials.

Table 2. Characterization of Water-Gas Shift Materials.

	Materials	Crystallite Size (XRD), nm	Multipoint BET Surface Area, m^2/g
I	Ceria (Carbonate Precipitation)	4.93 <220>	129.0
II	Ceria (Thermal Decomposition)	11.8 <220>	56.6
III	$Ce_{0.8}Sm_{0.2}O_{1.9}$	5.85 <220>	85.0
IV	$Ce_{0.8}Sm_{0.15}Gd_{0.05}O_{1.9}$	9.76 <220>	79.5
V	$Ce_{0.8}Sm_{0.15}Gd_{0.05}O_{1.9}$	8.99 <220>	94.3
VI	Au/ $Ce_{0.8}Sm_{0.15}Gd_{0.05}O_{1.9}$	6.74 (Au, <111>)	103.8

Table 3. Elemental Analysis of Doped Ceria Prepared by Carbonate Co-Precipitation.

	Atomic %		
Spot #	Ce	Sm	Gd
1	78.4	16.0	5.7
2	78.2	15.8	6.1
3	80.4	14.9	4.7
Average	79.0	15.6	5.5

Elemental analysis of the doped ceria by EDX (Table 3) shows that elemental compositions of Ce, Sm and Gd in the doped ceria matches the nominal compositions of the Ce^{3+}, Sm^{3+} and Gd^{3+} in the nitrate mixture. In other words, the atomic % of Sm and Gd in ceria can be achieved by mixing the nitrate solutions in a desired volumetric ratio. This is consistent with a recent paper in which a single lanthanide element is doped in the ceria[11]. Since the XRD pattern of the doped ceria prepared in this work matched the literature pattern of a fluorite structure[7], the composition of doped ceria was assigned to be $Ce_{0.8}Sm_{0.15}Gd_{0.05}O_{1.9}$. Our inductively coupled plasma mass spectroscopy (ICP-MS) results confirmed the materials composition of our doped ceria. And the atomic absorption spectroscopy (AAS) analysis quantified the gold content in the Au/$Ce_{0.8}Sm_{0.15}Gd_{0.05}O_{1.9}$ to be 7.1 wt %. If all the gold in solution are deposited onto the ceria, the gold content of our catalyst would be 7.6 wt %.

Some of the major limitations of commercial $Cu/ZnO/Al_2O_3$ water-gas shift catalysts include the thermal aging (or sintering) and the stability with water[12,13]. A recent study has suggested some deactivation mechanism of Au/CeO_2 catalysts[9]. Here, we investigated the effects of both thermal aging and water vapor on the Au/$Ce_{0.8}Sm_{0.15}Gd_{0.05}O_{1.9}$. These effects were examined simultaneously by flowing Ar gas (saturated with water) over the Au/$Ce_{0.8}Sm_{0.15}Gd_{0.05}O_{1.9}$ that was controlled at 350°C. Table 4 summarizes the durability test results of Au/$Ce_{0.8}Sm_{0.15}Gd_{0.05}O_{1.9}$ (Sample VII). Sample VII was prepared using Sample IV as the support material. The BET analysis showed that flowing humidified Ar over the Au/$Ce_{0.8}Sm_{0.15}Gd_{0.05}O_{1.9}$ at 350°C had insignificant effects on the BET surface area (Table 4). The change in surface area was less than 5% for 10 hours. Figure 1 illustrates a SEM image of the Sample IX. Other images of Samples IV, VII, VIII and IX with different magnifications (500x, 5000x and 50000x) are not shown here. The SEM images illustrates that there is no significant morphology difference among the samples. Particle size analysis with transmission electron microscopy (TEM) is shown in Figure 2. The TEM image suggests that the Au/$Ce_{0.8}Sm_{0.15}Gd_{0.05}O_{1.9}$ remains nanoscale after 10 hours.

Table 4. Durability of Au/ $Ce_{0.8}Sm_{0.15}Gd_{0.05}O_{1.9}$ under Humidified Argon Treatment at 350°C.

	Materials	Duration for Humidified Ar Treatment (hrs.)	Multipoint BET Surface Area, m^2/g
IV	$Ce_{0.8}Sm_{0.15}Gd_{0.05}O_{1.9}$	0	79.5
VII	Au/$Ce_{0.8}Sm_{0.15}Gd_{0.05}O_{1.9}$	0	75.1
VIII		3	78.7
IX		10	77.8

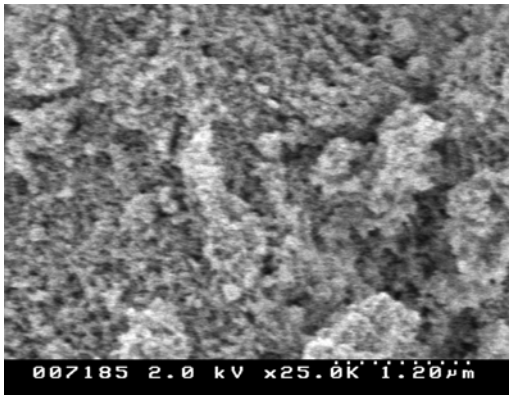

Figure 1. SEM micrograph of Au/ $Ce_{0.8}Sm_{0.15}Gd_{0.05}O_{1.9}$ treated with humidified Ar for 10 hrs at 350 ^oC (Sample IX).

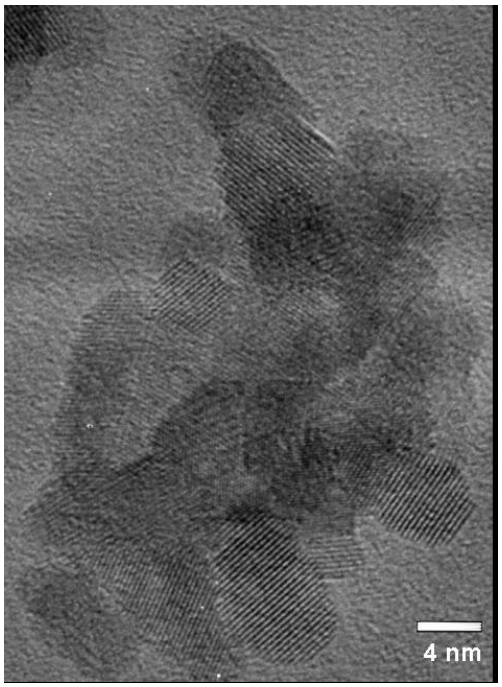

Figure 2. TEM micrograph of Au/ $Ce_{0.8}Sm_{0.15}Gd_{0.05}O_{1.9}$ treated with humidified Ar for 10 hrs at 350 ^oC (Sample IX).

The WGS reaction rates of ceria-based samples are compared in Figure 3. We kept the conversion < 10% and the pressure drop < 10 psig in all cases. Therefore, the catalyst bed temperature can be assumed to be constant, and mass transfer-free operating conditions are established for each temperature. We observe no methane in all our experiments. The BET surface area analysis results are shown in Table 5.

The activities of two Au/CeO2 catalysts are shown in Figure 3. The difference is the preparation of ceria, while the conditions of gold deposition are the same. Sample XI has a larger surface area and higher activity than Sample XII (Figure 3 and Table 5).

Although surface area and crystallite size are generally believed to be two of the major factors for catalytic activities, dopants in Ce crystal structure also play critical roles in the WGS activity. This work shows that nanocystalline (< 10 nm, XRD) Au/$Ce_{0.8}Sm_{0.15}Gd_{0.05}O_{1.9}$ with high surface area (>100 m^2/g) can be synthesized by carbonate co-precipitation followed by deposition with urea. As indicated in Tables 1 and 2, the surface area and the crystallite size are process-dependent. On the other hand, Au/$Ce_{0.8}Sm_{0.15}Gd_{0.05}O_{1.9}$ has a higher surface area than Au/$Ce_{0.75}Zr_{0.25}O_2$ (Table 4), but the latter is a better WGS catalyst below 400 ^oC (Figure3). To elucidate other important parameters, we have investigated the WGS activities of Mg-, Sm-, Gd- and Zr-doped ceria (Figure 3).

We demonstrated earlier that the additions of Sm and Gd into Ce crystal structure thermally stabilize the material, but these dopants apparently hinder the oxygen mobility (below 400°C). In contrast, Zr seems to improve both thermal resistance of the ceria and oxygen storage/release capacity. This is consistent with some general understanding of Ce-Zr materials[14,15]. On the other hand, Au/MgO has been shown to be a very active catalyst for CO oxidation[16], but there is no published result on its WGS activity. Here our results indicate that doping Mg into $Ce_{0.8}Sm_{0.15}Gd_{0.05}O_{1.9}$ structure greatly improves the WGS activity of Au/ $Ce_{0.8}Sm_{0.15}Gd_{0.05}O_{1.9}$. This implies that MgO improves the oxygen transport and the CO oxidation step in the WGS reaction. The TEM image of our Au/MgO/$Ce_{0.8}Sm_{0.15}Gd_{0.05}O_{1.9}$ is shown in Figure 4. The activity of this catalyst is shown in Figure 3.

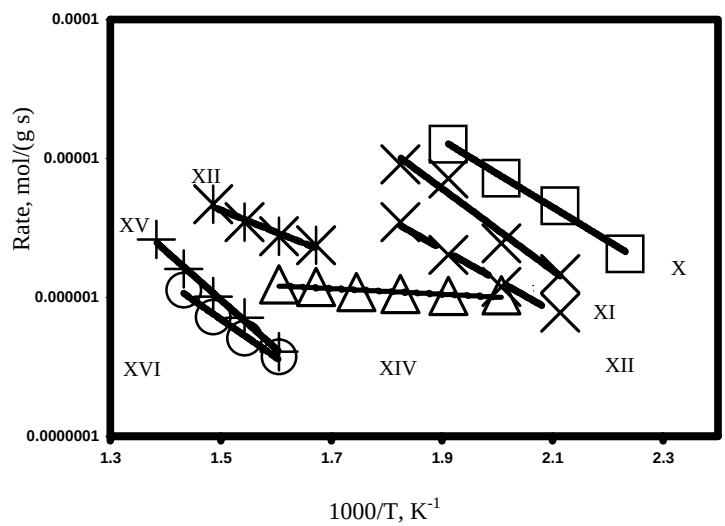

Figure 3. An Arrhenius plot for the water-gas shift rates on ceria-based catalysts (Samples X to XVI, Table 5). (Inlet gas contains 5%CO and 5%H_2, and H_2O(g)/CO=5.)

The significance of this work is that we have developed a non-pyrophoric low temperature WGS catalyst for fuel processor. Our catalysts have two important characteristics. First, all the catalysts shown in Figure 4 are not sensitive to air (i.e. non-pyrophoric) while typical Cu/ZnO/Al_2O_3 catalysts are air sensitive. In contrast to industrial plants, this feature is particularly important for objective force applications because these applications involve frequent on-off cycles during which air enters the system. Using non-pyrophoric materials often means a safer system. Another important characteristic is that our catalysts show high activities at H_2/CO ratio = 1. Previously, most of the water-gas shift catalyst research projects

focus on gas feed at very low or in absence of hydrogen. Only recently the literature[3,8] shows some interests in the water-gas shift catalyst that works at a reasonable hydrogen level (relative to CO). Note that hydrogen is the main fuel for fuel cell applications, particular polymer electrolyte membrane (PEM) fuel cells. Fuel processors break down the hydrocarbon fuel into reformate which contains smaller molecules including H_2, CO and others. Here we have tailored our catalysts at H_2/CO =1 which is realistic for catalytic partial oxidation of diesel fuel[1].

Table 5. Characterization of Ceria-Based WGS Catalysts Shown in Figure 3.

Sample	Materials	Preparation Method of Ceria or Doped Ceria	Multipoint BET Surface Area, m^2/g
X	$Au/MgO/Ce_{0.8}Sm_{0.15}Gd_{0.05}O_{1.9}$	Carbonate Coprecipitation	73.4
XI	Au/CeO_2	Carbonate Coprecipitation	94.9
XII	Au/CeO_2	Thermal Decomposition	70.1
XIII	$Au/Ce_{0.75}Zr_{0.25}O_2$	Sol gel	57.9
XIV	CeO_2	Carbonate (Co)Precipitation	129.0
XV	$Au/Ce_{0.8}Sm_{0.15}Gd_{0.05}O_{1.9}$	Carbonate Coprecipitation	103.8
XVI	$MgO/Ce_{0.8}Sm_{0.15}Gd_{0.05}O_{1.9}$	Carbonate Coprecipitation	73.8

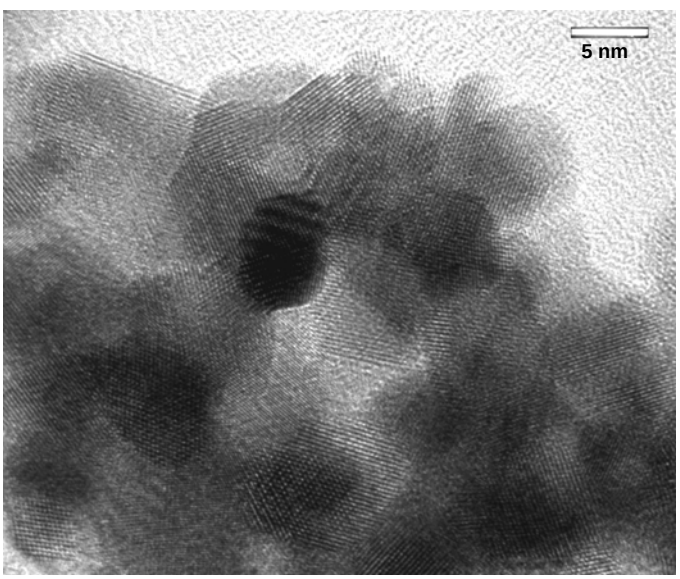

Figure 4. The TEM image of $Au/MgO/Ce_{0.8}Sm_{0.15}Gd_{0.05}O_{1.9}$.

Conclusions

We have developed a new water-gas shift catalyst, $Au/MgO/Ce_{0.8}Sm_{0.15}Gd_{0.05}O_{1.9}$, which is non-pyrophoric and has high WGS activities at low temperature (below 300 ^oC). This nanocystalline(<10nm) $Au/MgO/Ce_{0.8}Sm_{0.15}Gd_{0.05}O_{1.9}$catalyst was synthesized by carbonate co-precipitation of doped ceria followed by gold deposition with urea. The durability of Sm- and Gd-doped ceria as low-temperature water-gas shift (WGS) catalysts was tested with argon gas saturated with water at elevated catalyst temperatures. The SEM and BET surface area analysis indicated that there were no significant changes at 350°C for 10 hours. We have evaluated the WGS activities of various ceria-based catalysts containing Au, Sm, Gd, Zr and Mg. Our results indicate that the presence of Au and MgO in $Au/MgO/Ce_{0.8}Sm_{0.15}Gd_{0.05}O_{1.9}$ plays significant roles in the WGS reaction.

Acknowledgement. This work was supported by FY03 Army Research Laboratory Director's Research Initiative (DRI) Award. Dr. Mattew Ervin and Dr. Wendy Sarney have provided help in electron microscopy.

References

(1) Krummenacher, J. J., West, K. N. and Schmidt, L. D., *J. Catalysis* **2003**, *215*, 332.
(2) Cable, T. L., Brakas, A. B., Ruhl, R. C. and Milliken, C. E., US Patent 6,238,816 (**2001**).
(3) Fu Q, Saltsburg, H. and Flytzani-Stephanopoulos, M., *Science* **2003**, *301*, 935.
(4) Cameron, D., Holliday, R. and Thompson, D., *J. Power Sources* **2003**, *118*, 298.
(5) Sakurai, H., Ueda, A., Kobayashi, T. and Haruta, M., *Chem. Commun.* **1997**, *3* , 271.
(6) Andreeva, D., Idakiev, V., Tabakova, T., Ilieva, L., Falaras, P., Bourlinos, A. and Travlos, A., *Catalysis Today* **2002**, *72*, 51.
(7) Fu, Q., Weber, A. and Flytzani-Stephanopoulos, M., *Catalysis Letters* **2001**, *77*, 87.
(8) Zalc, J. M., Sokolovskii, V. and Loffler, D. G., *J. Catalysis* **2002**, *206*, 169.
(9) Kim, C. H., Bej, S. K. and Thompson, L. T., AIChE 2002 Annual Conference.
(10) Pati, R. K., Lee, I. C., Chu, D. and Ehrman, S. H., *Preprint Paper-American Chemical Society, Division of Fuel Chemistry* **2003**, *48*, 812.
(11) Li, J., Ikegami, T., Mori, T. and Wada, T., *Chem. Mater.* **2001**, *13*, 2913.
(12) Twigg, M. V. and Spencer, M. S., *Applied Catalysis A: General* **2001**, *212*, 161.
(13) Lindstrom, B. AND Pettersson L. J., *Catalysis Letters* **2001**, *74*, 27.
(14) Duprez, D. and Descorme, C. In *Catalysis by Ceria and Related Materials*; Trovarelli, A. , Ed.; Imperial College Press: London, 2002; pp. 243-280.
(15) Trovarelli, A., Boaro, M., Rocchini, E., de Leitenburg, C. and Dolcetti, G., *J. Alloys and Compounds* **2001**, *323*, 584.
(16) Guzman, J. and Gates, B. C., *J. Phys. Chem. B* **2002**, *106*, 7659.

CATALYTIC NANOCOMPOSITE MEMBRANES FOR CO ABATEMENT IN FUEL CELL APPLICATIONS

K. A. Carrado[1], R. Kizilel[2], G. Sandi[1], S. Seifert[3] C. L. Marshall[4], M. J. Castagnola[4]

[1]Chemistry, [3]Experimental Facilities and [4]Chemical Engineering Divisions, Argonne National Laboratory, 9700 S. Cass Ave., Argonne, IL, [2]Chemical & Environmental Engineering Dept., Illinois Institue of Technology, 10W 33rd Street, Chicago, IL

Abstract

Catalytic nanocomposite membranes have been prepared by ion exchanging Pt^{2+} for Li^{+} in a synthetic hectorite clay and dispersing this inorganic component within a polymeric matrix. Transparent, self-supporting membranes from the polymer-clay nanocomposite are then made. The reduction of Pt^{2+} to Pt(0) nanoclusters is accomplished by thermal reduction under H_2 at temperatures higher than 120°C. Loadings are in the 1-2 wt% Pt range. The size of the Pt(0) nanoparticles is determined by in situ small angle x-ray scattering (SAXS) techniques at about 5 nm. The membranes are stable to 200°C. These membranes have been tested for H_2 and CO diffusion at room temperature. Without any other reactive gases present (such as O_2), a selectivity enhancement from 1:1 to 3:1 H_2:CO is observed through the membrane.

Introduction

A major hurdle in current fuel cell technology is to provide a high purity gas feed. Fuel cells that operate at relatively low temperatures (<130°C) are adversely affected by even low levels of carbon monoxide (CO). Production of H_2 from the reforming of natural gas (or possibly other carbon reserves) and the water gas shift reaction yields CO as a byproduct at levels that poison fuel cell anodes. Therefore, additional technology is required to decrease the CO to ppm levels.

Current methods for removing residual CO include pressure-swing adsorption, preferential oxidation, and catalytic methanation, all of which add cost and complexity to the fuel processing system[1]. A call for basic research to supply alternative solutions to this problem was recently made, including more active catalysts for the low-temperature water-gas shift reaction, better gas stream separation processes and membranes, and CO-tolerant catalysts at the fuel cell anode[1].

We are currently testing the separation and oxidation of CO from a H_2-rich gas by taking advantage of decreased permeation of CO over H_2 through a polymer-clay nanocomposite membrane and simultaneous catalytic CO oxidation via Pt(0) nanoclusters that are supported by the membrane. It is envisioned that such a membrane would be placed just before the fuel cell.

Experimental

Synthesis of Catalytic Membranes. The preparation of synthetic lithium hectorite (SLH) clay has been reported in detail[2]. Loading of Pt(II) is accomplished by adding 0.5 gm SLH to a 2.5 mM aqueous $Pt(NH_3)_4Cl_2$ solution and stirring for 24 hr. This yields a material that has 65% of the cation exchange capacity loaded with Pt(II), or 4.65 wt% Pt. The desired amount of poly(ethylene oxide) (PEO) is then added and the mixture is stirred for another 24 hr, with a final loading of 2.4 wt% Pt on a 1:1 nanocomposite. Films were prepared by puddle-casting the slurries onto Teflon-coated glass plates and air-drying. Further drying is carried out at 120°C under an inert atmosphere for 24 hr. The ion-exchanged membrane is then reduced in a flow of H_2 at 200°C for 3 hr.

In Situ Small Angle X-Ray Scattering (SAXS). *In situ* SAXS was carried out at the Sector 12 of the Advanced Photon Source at Argonne National Laboratory. Monochromatic x-rays (18 keV) were scattered and collected on a 15 x 15 cm^2 CCD camera. The scattering intensity is corrected for adsorption and instrument background. The differential scattering cross section is expressed as a function of scattering vector *q*. The value of *q* is proportional to the inverse of the length scale ($Å^{-1}$). The instrument was operated with a sample to operator detector distances of 228 cm and 390 mm to obtain data at $0.01 < q < 0.3$ $Å^{-1}$ and at $0.08 < q < 2.3$ $Å^{-1}$, respectively. For these studies, a specially designed sample holder was used to heat the sample and collect SAXS data at the same time. Films of about 1.25 cm in diameter and 40 □m in thickness were placed in the sample holder and held using Kapton tape. The furnace temperature program was set to ramp from room temperature to 200°C at 5°C/min, and the gas flow of H_2 and He was started at room temperature.

Reactor Design. A new s.s. tubular reactor that consists of a catalytic membrane in the middle of the reactor standing perpendicular to flow was designed. Special temperature-resistant O-rings were used to eliminate the possible leaks during the experiments. The experimental setup consists of a reactor, a feed and exhaust lines, flow meters, flow controllers, temperature controller, and safety and check valves (see Figure 1). Gases are fed into the reactor tube and the temperature can ramp to 250ºC. A thermocouple is placed in the reactor bed. The reactor is housed in a clamshell furnace controlled by an Omega oven controller (TIC-500) equipped with a temperature limit switch set for 30ºC higher than the reaction temperature. From the reactor tube, the feed gas flows into saltwater/ice bath where the products and remaining reactants are condensed and collected for analysis. The collector can be isolated from the reactor and removed to collect the sample. The reactor is designed to handle a variety of conditions under continuous flow conditions at ambient pressure. The feed from the top of the reactor consists of He, CO, and H_2. The oxygen source will be air added in countercurrent flow with respect to CO and H_2.

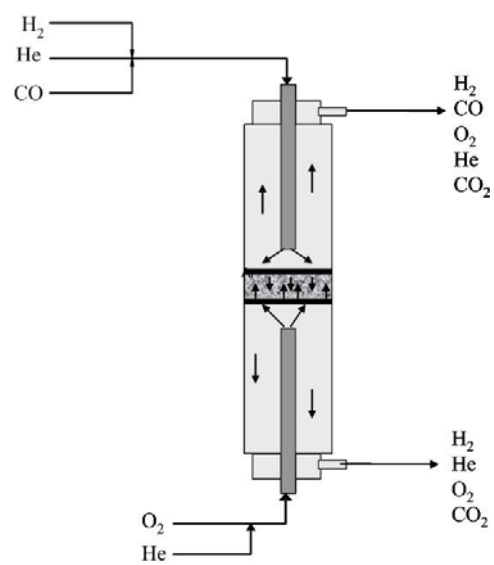

Figure 1. Reactor design for testing of catalytic membranes.

Results and Discussion

In Situ Pt Reduction. The Pt^{2+} reduction process was monitored under either H_2 (reducing) or He (inert) flow at different temperatures with simultaneous collection of SAXS data. When the

membranes were heated under a He flow (see Figure 2), the SAXS data could be fit using one structural layer throughout the entire temperature range in the so called general unified fit (GUF). This fitting procedure is explained in detail by Beaucage et al.[3]:

$$I(q) \approx G\exp\left(\frac{-q^2R_g^2}{3}\right) + B\left[\frac{\left(erf\left(qR_g/\sqrt{6}\right)\right)^3}{q}\right]^P$$

where G is the Guinier prefactor, B is the prefactor specific to the type of power-law scattering, q is the momentum transfer, Rg is radius of gyration and P is a constant. The derived Rg values are provided in Table 1.

This is a general equation developed to describe scattering functions that contain multiple length-scales (Guinier regimes) separated by power-law scattering regimes. Under He, scattering from the membrane itself should dominate. In contrast to the results with He, the addition of H_2 at relatively high temperatures produces significant changes in the SAXS results (see Figure 3). Under these conditions, the data fit better to two structural levels, with an additional length-scale added as seen in Table 1. This is presumbed to arise from the reduction of Pt^{2+} to Pt(0) nanoclusters. Harrison et al.[4] have claimed that the reduction of Pt^{2+} occurs at 140°C. Our SAXS measurements indicate that Pt(0) nanoparticles with a diameter of 4.8 nm form at 120°C. Diameters of the particles are calculated by multiplying the radius of gyration, which is derived from fitting results, by a constant of 2.6 (Rg = R/1.29 for spherical particles). The results also show that further heating to 200°C does not form significantly larger agglomerates.

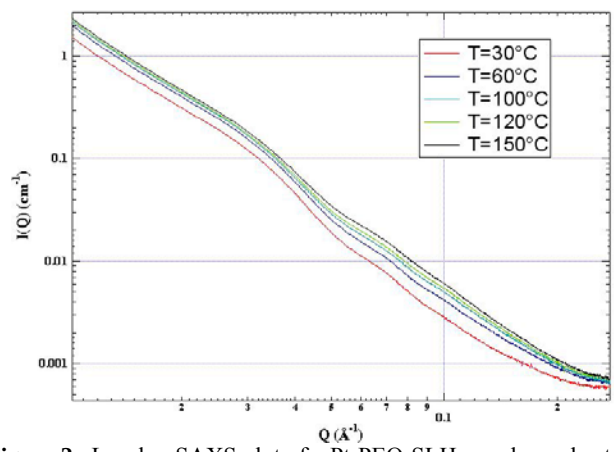

Figure 2. Log-log SAXS plot of a Pt-PEO-SLH membrane heated to various temperatures under He (non-reducing) flow.

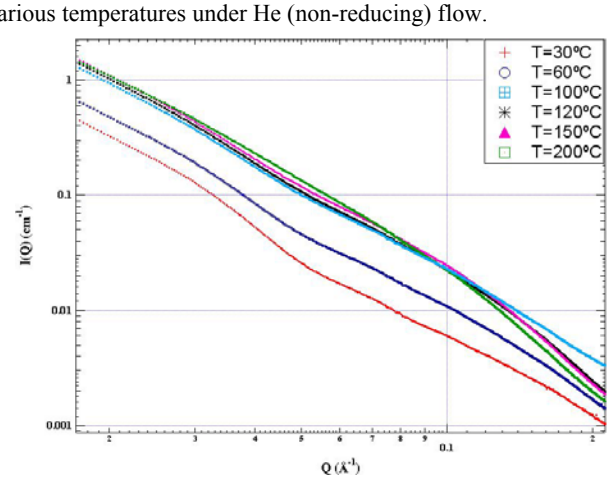

Figure 3. Log-log SAXS plot of a Pt-PEO-SLH membrane heated to various temperatures under H_2 flow.

Table 1. Microstructural Beaucage GUF SAXS Analysis of Pt-PEO-SLH Catalytic Membranes under Various Atmospheres

	Rg (Å)		
Temp. (°C)	He	H_2	
	Layer 1	Layer 1	Layer 2
30	81.3	80.0	-
60	79.2	81.9	-
100	79.7	84.2	-
120	81.7	88.1	18.6
150	82.0	90.5	19.0
200	89.8	104.7	19.8

Membrane Testing for H_2 and CO Performance. H_2-rich gas is fed from one end of the reactor. Permeation through the membrane alone acts to reduce the CO concentration. A selectivity enhancement from 1:1 H_2:CO to 3:1 H_2:CO has been observed upon feeding through a reduced Pt-PEO-SLH membrane at room temperature. Future experiments will feed a dilute CO stream with a countercurrent flow of O_2 at elevated temperature to convert the CO to CO_2 catalytically. The rates of CO oxidation depend on a variety of factors such as the thickness of the catalyst layer, its catalytic activity, and reaction conditions. Experimentation is directed toward formulating, evaluating, and establishing catalytic solids that promote the oxidation of CO with O_2.

Conclusions

A Pt-PEO-SLH catalyst is reduced successfully by thermal reduction under a H_2 flow at temperatures higher than 120°C. SAXS results (not shown) confirm that the reduction process does not degrade the polymer structure, although the polymer relaxes from crystalline to amorphous at >60°C. At low temperatures, CO poisons Pt(0). This is unfortunate because at higher temperature, Pt(0) is active for the catalytic oxidation of CO to CO_2. This is a higher temperature reaction than the operating temperature of low-temperature (<130°C) fuel cells, however, so this reaction cannot be exploited in current cells. It is envisioned that by using a membrane separator outside of the fuel cell, the possibility of catalytic oxidation of CO becomes a possibility. Low-temperature fuel cells are unstable above 135°C because of the Nafion. The PEO-membranes described here can go to 200°C. In the future, more thermally stable polymers will be tested. Pure clay could be used (laponite makes excellent films, for example), but the speculation is that the polymer helps to solvate the metal clusters and keep them from aggregating[5].

Acknowledgement. S. Landers fabricated the reactor flow cell. This work was performed under the auspices of the U.S. Department of Energy, Office of Basic Energy Sciences, Division of Chemical Sciences, Geosciences, and Biosciences under contract number W-31-109-ENG-38.

References

1. "Basic Research Needs for the Hydrogen Economy", report from the DOE-BES Workshop on Hydrogen Production, Storage, and Use, held May 13–15, 2003; available on www.sc.doe.gov/bes.
2. Carrado K. A., *Appl. Clay Sci.*, **2000**, *17*, 1.
3. Beaucage G., Schaefer D. W. *J. Non-Cryst. Solids*, **1994**, *172-174*, 797.
4. Harrison J. B., Berkheiser V., Erdos G. W., *J. Catal.*, **1988**, *112*, 126.
5. P. Balbuena, personal communication.

DEFECT-FREE ZEOLITE THIN FILM MEMBRANES FOR H_2 SEPARATION

Margaret E. Welk and Tina M. Nenoff*

Chemical and Biological Technologies, Sandia National Laboratories, P.O. Box 5800, MS 0734, Albuquerque, NM 87185-0734, USA E-mail: mewelk@sandia.gov.

Introduction

Much effort has recently been devoted to the synthesis of inorganic zeolite membranes because of their potential applications in the domains of gas separation, pervaporation, reverse osmosis or in the development of chemical sensors and catalytic membranes.[1,2,3,4,5] Specifically, development of new technologies for H_2 separation and purification has a high priority for the future of H_2 as a fuel source. H_2 is commonly produced by the reformation of hydrocarbons and must be purified. Zeolite membranes in particular combine pore size and shape selectivity with the inherent mechanical, thermal, and chemical stability necessary for long term separations.

The effective pore size distribution of the zeolite membrane, and hence its separation performance, is intrinsically governed by the choice of the zeolitic phase.[6,7,8,9] This applies when molecular size exclusion sieving is dominant and no other diffusion pathways bypass the network of well defined zeolitic channels; otherwise viscous flow through grain boundaries prevails. Zeolite membranes are typically synthesized on porous substrates by two different methods,[10]: one step hydrothermal reaction on a pristine substrate from an aluminosilicate gel or by seed-promoted hydrothermal crystallization of the zeolitic layer. In both cases, the synthesis is affected by many complex interrelated factors such as the overall composition, concentration and viscosity of the gel, its pH, the source of silica and its degree of polymerization, the temperature and duration of the reaction. The optimization of these parameters is crucial to obtaining reliably "defect free" membranes. We report here on the synthesis of ZSM-5 and silicalite membranes[11] on porous alumina disk supports, their characterization and their permeation performance for pure He, SF_6, H_2, CO_2, O_2, CH_4, N_2, and CO gases. We also show the reproducibility of the permeation values and the durability of a number of these films.

Experimental

Gases: Reagent grade pure gases were purchased from Trigas. H_2, CO_2, O_2, CH_4, N_2, CO were used to test the permeation of the membranes for reforming gases. SF_6 was used to detect defects, He was used to purge and clean the unit.

Permeation Measurements: The membrane permeations were measured at room temperature using pure gases and a constant trans-membrane pressure of 16 PSI controlled by a backpressure regulator. The membrane was sealed in a Swagelok fitting using Viton O-rings. The gas flow through the membrane was measured using an acoustic displacement flowmeter (ADM 2000 from J&W) and a digital bubble flowmeter (HP-9301). Between permeation measurements with different pure gases (SF_6, H_2, CO_2, O_2, CH_4, N_2, CO), the whole system is purged, flushed with Helium and evacuated several times. The ideal gas selectivity was calculated as the ratio of the permeances in the steady regime.

Characterization Techniques: The zeolite membranes and seeds were characterized by X-ray diffraction (Siemens D500 diffractometer, Cu Kα radiation, Bragg-Brentano geometry) and by Scanning Electron Microscopy (JEOL–6300V equipped with a Link Gem Oxford 6699 EDAX attachment).

Membrane Synthesis: In this work, the growth of both the ZSM-5 and silicalite (Al-free ZSM-5) membrane on the porous support is achieved by hydrothermal synthesis on supports seeded by rubbing.

The α-alumina substrates supplied by Inocermic Gmbh have a 1.8 micron average pore size, a diameter of 13 mm and a thickness of 1mm. The alumina substrates were first cleaned ultrasonically in acetone, rinsed in DI water and calcined at 1000°C overnight to remove any contaminants. All membranes in this work were obtained using seeded substrates to promote the nucleation and growth of the zeolite layer.

Tetra Propyl Ammonium (TPA) templated silicalite seeds were prepared under mild hydrothermal conditions in order to limit the size of the crystallites.[12] A rubbing method of seeding was used. The seeded alumina substrates were then heated in air to 500°C for 6 hours, and then cooled to room temperature using a ramp rate of 4°C /min to remove the TPA template and attach the seeds to the substrate. They were then stored in a desiccator for later use.

The difference in zeolite type resulted from the type of gel used for the hydrothermal synthesis. For ZSM-5, water, sodium hydroxide and alumina sulfate were mixed together and stirred until all reactants dissolved. Ludox-30 (Aldrich) was added to the mixture, which was then aged hours at room temperature for 24 hours. For Silicalite, the silicon source for the membrane synthesis is colloidal silica Ludox SM-30 (Aldrich); the organic template used is Tetra Propyl Ammonium (TPA) from TPAOH and TPABr (both from Alfa Aesar), and NaOH is the alkalinity source. Each gel was aged while being stirred at room temperature for 24 hours.

The seeded substrates were held vertically in the Teflon lined Parr reactor using Teflon holders to prevent sedimentation on top of the membrane. The homogenous gel was then poured in the reactor until the membrane was fully immersed. The hydrothermal syntheses were carried out in Parr reactors with a 23ml Teflon liner at temperature ranging from 160°C to 180°C and reaction time from 12 hours to 48 hours.

After synthesis, the membrane was washed with DI water and dried in air at 50°C for few hours. A permeation test on the as synthesized membrane allows the rapid assessment of its quality before the time-consuming calcination step. At that stage, a good quality membrane should be gas-tight, or impermeable, for SF_6. The SF_6 kinetic diameter of 5.5 Å is slightly larger than the pores of the ZSM-5 zeolite (minimum diameter 5.1 Å) thus SF_6 diffusion indicates the presence of membrane defects.[13] Any existing defects (partial coverage of the substrate and micro-cracks) can be repaired by a second hydrothermal synthesis step, using a shorter reaction time and more diluted starting gel. These modifications to the original synthesis parameters help to avoid the growth of columnar zeolite crystals (or agglomerates of crystals) on top of the first layer, as they would not contribute to the plugging of the existing cracks or voids in the film. The silicalite membranes presented here were gas-tight prior to calcination and did not require a second hydrothermal treatment.

Once the adequacy of the membrane was established, the organic template was removed from the membrane pores by calcination in air. The calcined membranes are whitish in color, indicating that no carbon deposit is present on the surface.

Results and Discussion

Examination of the membranes by SEM showed dense coverage of zeolite crystals on the alumina support. The thickness of the crystalline layer is on average 10 microns and was found to be fairly uniform throughout the individual membranes. Selectivity values are listed in Tables 1 and 2.

ZSM-5: For H_2 purification, ZSM-5 membranes were synthesized on flat α-alumina disks. They were tested for selectivities toward the pure gases. Much as expected, the permeation preferences were dictated by size selectivity; He > H_2 > CO_2 > O_2 > N_2 > CO > CH_4. In particular, these membranes have separations of $H_2/N_2 \geq 61$, $H_2/CO_2 \geq 80$, $H_2/CH_4 = 7$, $CH_4/CO_2 \geq 11$. Although these membranes required additional secondary growth procedures to produce a "defect-free" membrane, the flux through the films was extremely high, on the order of 10^{-6} mole/(m^2Pa sec).

Investigation of the performance and longevity at room temperature of the ZSM-5 membranes showed a moderate decrease over time. After more than 60 hours of continuous measurement under H_2, the flow rate was about 85% of its peak flow value. Calcination to 500°C restores the ZSM-5 membrane to its original flow value. Most likely, water vapor that was not removed from the permeation unit during the He gas purge and evacuation step is responsible for this decrease in flow. Longevity tests continue with other pure gases as well as industrially important mixed gases.

Silicalite: An interesting feature of these membranes is that the permeance with CO_2 is higher than that of any other gas tested, including He or H_2, even though the kinetic diameter of CO_2 is significantly larger than that of He or H_2. This property is observed reproducibly for every silicalite membrane synthesized and tested in our lab. As the CO_2 to air permeance ratios we observed are between 2 and 3, and CO permeances up to 6×10^{-7} [mole/m^2 s Pa] our membranes could at room temperature separate CO_2 from air. The higher permeance of CO_2 than other gases is likely due to surface diffusion of the CO_2 (coexisting with Knudsen diffusion), which has apparently a good affinity for this zeolite surface.

We tested a broad series of light gases (He, SF_6, H_2, CO_2, O_2, CH_4, N_2, and CO), targeting those associated with methane reforming for H_2 production. Results show that methane exhibits a behavior similar to that of CO_2, diffusing faster than both He and H_2, although the enhancement is less pronounced. CO does not seem to interact strongly with the membrane, with permeance values very similar to those of O_2 or N_2.

Investigation of the performance durability and longevity of the silicalite membranes showed that the permeance for CO_2 decreases slowly with time. After more than 60 hours of continuous measurement under CO_2, one of the membranes (22B) showed only about a third of the initial flow value. The non-interacting gases such as He do not show a marked reduction in permeance over time. Importantly, the membrane could be partially "regenerated" by heating it with a temperature profile similar to that employed for the initial calcinations. The gas flow increased to about half the starting values. This gradual decrease of permeance with time observed with pure gas will likely occur over a longer time scale when gas mixtures are used.

Conclusions

"Defect-free" ZSM-5 and Silicalite membranes have been grown reproducibly through experimentation with the synthetic parameters. The membranes are of uniform thickness and good quality as shown by the consistency and quality of the permeation data and the low SF_6 permeance. Although ZSM-5 and Silicalite are structurally identical (ZSM-5 has substituted aluminum into a portion of the silicon framework sites), they show remarkably different permeation properties. The permeation characteristics of silicalite membranes show an interesting preference for pure CO_2 gas, which flows through the silicalite membranes faster than He gas or H_2 gas, despite the larger kinetic diameter of CO_2. Modifications of the permeation unit to allow the use of gas mixtures at different temperatures are in progress and will allow the determination of the best regime for these membranes.

Acknowledgement. Sandia is a multiprogram laboratory operated by Sandia Corporation, a Lockheed Martin Company, for the United Stated Department of Energy's National Nuclear Security Administration under contract DE-AC04-94-AL85000. We thank the DOE/Hydrogen, Fuel Cells, and Infrastructure Technologies Program for continued funding.

Table 1. ZSM-5 and Silicalite Single Gas Selectivities. Trans-membrane pressure: 16 PSI.

SNL TPA/Si (Silicalite 2-sided) ≈ 10^{-6} – 10^{-7} mole/(m^2 Pa sec)

$H_2/N_2 = 1.4$	
$H_2/CH_4 = 0.625$	$CO_2/N_2 = 4.2$
$He/N_2 = 1.1$	$CO_2/O_2 = 4.9$
$CH_4/N_2 = 2.28$	$CO_2/H_2 = 3.0$
$H_2/CO_2 \geq 0.34$	$CO_2/CO = 4.2$
$H_2/O_2 = 1.7$	$CO_2/CH_4 = 1.8$
$CH_4/CO_2 = 0.54$	
$H_2/CO = 1.43$	

SNL Na/Al/Si (ZSM-5 2-sided) Knudsen Selectivity Lit. (values for Al/Si) ≈ 10^{-6}mole/(m^2 Pa sec) ≈ 10^{-7}-10^{-10} mole/(m^2Pa•s)

$H_2/N_2 \geq 61$	$H_2/N_2 = 3.73$	$H_2/N_2 = 3.91$
$H_2/CH_4 = 7$	$N_2/CO_2 = 1.00$	$N_2/CO_2 = 0.625$
$He/N_2 \geq 7$	$He/N_2 = 2.64$	$H_2/N_2 = 100$; 150°C
$CH_4/N_2 \geq 1.4$	$CH_4/N_2 = 1.32$	10^{-10} perm.
$H_2/CO_2 \geq 80$		
$H_2/O_2 \geq 11$		
$CH_4/CO_2 \geq 11$		

Table 2. Silicalite Single Gas Permeance (10^{-7} mole/ m^2 s Pa). Trans-membrane pressure: 16 PSI.

Gas / (Kinetic ∅ (Å)) Membrane	He (2.6)	SF_6 (5.5)	H_2 (2.8)	CO_2 (3.3)	O_2 (3.5)	CH_4 (3.8)	N_2 (3.6)	CO (3.7)
18A	1.8	<0.05	2.4	2.9	1.4	-	-	1.6
21A	1.2	<0.04	1.6	3.0	1.3	1.7	1.1	-
22A	1.5	<0.02	2.0	5.9	1.2	3.2	1.4	1.4
22B	1.5	<0.03	2.9	4.9	-	-	-	-
22B regenerated	1.1	-	1.4	2.9	-	-	-	-
28A	0.8	<0.03	1.9	5.1	1.3	2.6	1.6	1.6

References

(1) Armor, J. N. *J. Membr. Sci.* **1998**, *147,* 217.
(2) Caro, J.; Noack, M.; Kolsch, P.; Schafer, R. *Microp. Mesop. Mat.* **2000**, *38,* 3.
(3) Chiang, A. S. T.; Chao, K-J. *J. Phys. Chem. Solids* **2001**, *62*, 1899.
(4) Noack, M.; Kolsch, P.; Schafer, R.; Toussaint, P.; Caro, *J. Chem. Eng. Technol.* **2002**, *25*, 221.
(5) Thoma, S. G.; Trudell, D. E.; Bonhomme, F.; Nenoff, T. M. *Microp. Mesop. Mat.* **2001**, *50*, 33.
(6) Vroon, Z. A. E. P.; Keizer, K.; Gilde, M. J.; Verweij, H. Burggraaf, A. J. *J. Membr. Sci.* **1996**, *113,* 293.
(7) Geus, E. R.; den Exter, M. J.; van Bekkum, H. *J. Chem. Soc. Faraday Trans.* **1992**, *88*, 3101.
(8) Bakker, W. J. W.; Kapteijn, F.; Poppe, J.; Moulijn, J. A. *J. Membr. Sci*. **1996**, *117*, 57.
(9) Bai, C.; Jia, M-D.; Falconer, J. L.; Noble, R. D. *J. Membr. Sci.* **1995**, *105,* 79.
(10) Lin X.; Kita, H.; Okamoto K-I. *Ind. Eng. Chem. Res.* **2001**, *40,* 4069.
(11) Bonhomme, François; Welk, Margaret E.; Nenoff, Tina M. *Microp. Mesop. Mat.* **2003**, *66,* 181.
(12) Persson, A. E.; Shoeman, B. J.; Sterte, J.; Otterstedt, J. E. *Zeolites* **1994**, *14*, 557.
(13) Breck, D.W. *Zeolite Molecular Sieves*, John Wiley and Sons, New York 1997.

NANOSTRUCTURED ELECTRODES FOR HYDROGEN FUEL CELLS

*Mahesh Waje, Cheng Wang, Jason M. Tang, , Yushan Yan**

Department of Chemical and Environmental Engineering, College of Engineering – Center for Environmental Research and Technology, Center of Nanoscale Science and Engineering, University of California, Riverside, CA 92521

* Corresponding author, email: Yushan.Yan@ucr.edu

Introduction

As a potential candidate for an environmentally benign and a highly efficient electric power generation technology, hydrogen fuel cells, a type of proton exchange membrane fuel cells (PEMFC) are now attracting enormous interest for various applications such as low/zero-emission vehicles, distributed home power generators, and power sources for small portable electronics.[1-4] One of the challenges in the commercialization of PEMFCs is the high cost of noble metals used as catalyst (e.g., Pt). Decreasing the amount of Pt used in a PEMFC via the increase of the utilization efficiency of Pt has been one of the major concerns during the past decade.[5] To effectively utilize the Pt catalyst, the Pt must have simultaneous access to the gas, the electron-conducting medium, and the proton-conducting medium. In the catalyst layer of a Pt-based conventional fuel cell prepared by the ink-process, the simultaneous access of the Pt particle by the electron-conducting medium and the proton-conducting medium is achieved via a skillful blending of Pt-supporting carbon particles and Nafion. The carbon particles conduct electrons and the Nafion conduct protons. However, even with the more advanced conventional electrodes, there is still a significant portion of Pt that is isolated from the external circuit and/or the PEM, resulting in a low Pt utilization. For example, Pt utilization in current commercially offered prototype fuel cells remains very low (20-30%) although higher utilization has been achieved in laboratory devices. Efforts directed at improving the utilization efficiency of the Pt catalyst have focused on finding the optimum material configurations while minimizing the Pt loading and satisfying the requirements of proton access, gas access, and electronic continuity. In the conventional ink-process, a common problem has been that the necessary addition of Nafion for proton transport tends to isolate carbon particles in the catalyst layer, leading to poor electron transport.

Due to their unique structural, mechanical, and electrical properties, carbon nanotubes have been recently proposed to replace traditional carbon powders in PEMFCs and have been demonstrated by making membrane electrode assemblies (MEA) using a carbon nanotube powder through a conventional ink process.[6-8] However, their results did not show many advantages over carbon black (Vulcan XC-72) since the Pt utilization within the PEMFC catalyst layer remained unaddressed. Growing carbon nanotube arrays directly on the carbon paper and then subsequently electrodepositing the Pt selectively on the carbon nanotubes promises to improve the Pt utilization, thus securing the electronic route from Pt to the supporting electrode in a PEMFC. The use of carbon nanotubes and the resulting guaranteed electronic pathway eliminate the previously mentioned problem with conventional PEMFC strategies where the Nafion would isolate the carbon particles from the electrode support. Eliminating the isolation of the carbon particles from the electrode support would thereby improve the utilization rate of Pt.

Generally, there are two categories of carbon nanotubes: single-walled nanotubes (SWNTs) and multi-walled nanotubes (MWNTs). A SWNT is a single graphene sheet rolled into a cylinder. A MWNT is comprised of several coaxially arranged graphene sheets rolled into a cylinder. According to theoretical predictions, SWNTs can be either metallic or semiconducting depending on the tube diameter and helicity.[9] The semiconducting band gap is proportional to the reciprocal diameter, 1/d, and the band gap becomes comparable to thermal energies at room temperature when a nanotube diameter is around 3 nm.[10] Whereas for the MWNTs, scanning tunneling spectroscopy (STS) measurements indicate that the conduction is mainly due to the outer shell,[11] which are usually larger than 3nm. Therefore, MWNTs should have a relatively high electrical conductivity at room temperature. In this paper, we will focus on MWNTs as a support for the Pt catalyst in PEMFCs because current synthetic methods for MWNTs are simpler than those for SWNTs.

Earlier attempts to deposit MWNTs on carbon paper were conducted by S. Désilets and his group,[12,13] who dipped carbon paper in a solution containing silica and Group VIII metal salts and used this silica gel on carbon paper to catalyze the growth of the MWNTs on the carbon paper by an ohmic heating process. Although MWNTs are firmly attached on the carbon paper, electrical contact between the MWNTs and the carbon paper could be hindered by the existence of silica. Our group is currently working on fuel cells that use MWNTs as a Pt catalyst support by directly growing MWNTs on carbon paper through a chemical vapor deposition (CVD) process using electrodeposited Co as the catalyst for MWNT growth and subsequently depositing Pt catalyst selectively on these MWNTs. This non-ink process ensures that all of the electrodeposited Pt catalyst particles are electronically accessible to the external circuit of a PEMFC.

Experimental

MWNT synthesis on carbon paper. The Co catalyst for MWNT growth is electrodeposited on one side of the carbon paper by a three-electrode dc method in a 5 wt. % $CoSO_4$ and 2 wt. % H_3BO_3 solution at 20ºC.[14] The deposition potential is 1.0 V vs SCE (saturated calomel electrode). The loading of Co is varied from 0.26 to 20 mg/cm^2 by controlling the total charge deposited assuming 100 % yield of the electrodeposition.

The MWNTs were grown with a chemical vapor deposition (CVD) procedure described elsewhere[16] with slight modifications. Carbon paper with Co electrodeposited on one side of the paper was placed in a furnace at ambient pressure and heated to 550ºC in 3 hrs under a 150 sccm N_2 flow and 7.5 sccm H_2 flow. These conditions were maintained for 30 minutes. The temperature was then raised to 700ºC over a 30 minute time interval. Upon reaching 700ºC, acetylene was introduced at 7.5 sccm for 1hr to facilitate MWNT growth. Finally, the acetylene and H_2 flow was cut off and the furnace cooled to room temperature in 150 sccm N_2 flow.

Pt deposition and MEA preparation. Following the CVD growth of the MWNTs, Pt was electrodeposited on the MWNTs by a three-electrode dc method in 5 mM H_2PtCl_6 and 0.5 M H_2SO_4 aqueous solution.[17] The deposition potential used was 0 V vs. SCE (saturated calomel electrode, Aldrich) and the loading of Pt was controlled by the total charge applied.

An MEA was prepared using two such MWNT-carbon paper composite electrodes by first immersing the two electrodes into 5% commercial Nafion solution for 30 mins and subsequent hot pressing these two electrodes with a Nafion 115 membrane in between the two electrodes.

Characterization. The carbon paper samples with electrodeposited Co, the subsequent MWNT/carbon paper samples and the Pt electrodeposited electrode samples were characterized by SEM (Philips XL30-FEG). MWNTs were further characterized by TEM (Philips CM300). Brunauer-Emmett-Teller method (Micromeritics ASAP 2010) was used to determine the surface area of MWNTs and carbon paper. The MWNT-carbon paper composites were tested by cyclic voltammetry in 5mM potassium ferricyanide (III) solution to determine the active surface area.

The performance of MEA prepared was tested using a fuel cell test station (ElectroChem. Inc., USA).

Results and Discussion

Figure 1 shows the SEM images of the carbon paper with and without electrodeposited Co. The carbon paper is made of fibers having a diameter between 5 and 10 µm (inset in Figure 1A) and the surface of the carbon fiber is clean before deposition. The hydrophobic property of carbon paper enables the selective deposition of Co on the side of the carbon paper facing the electrolyte solution, which also makes it possible for selective growth of MWNTs on one side of carbon paper. This is also necessary for fuel cell applications because further selective deposition of Pt catalyst becomes feasible. After applying 2 coulombs charge on 2.55 cm^2 circular carbon paper for depositing cobalt, which equals 0.26 mg/cm^2 of Co loading, nanocrystalline Co could be found on the surface of carbon fibers (Figure 1A). The particle size is in the range of 20 to 50 nm. With the increase of Co loading, the particle size increases. We observed dendrimeric nanocrystalline Co (Figure 1B) when the loading was 4 mg/cm^2. Further increases in loading, for example to 20 mg/cm^2 as shown in the inset of Figure 1B, made it possible to cover and connect the carbon fibers on the whole surface of carbon paper by a porous Co structure.

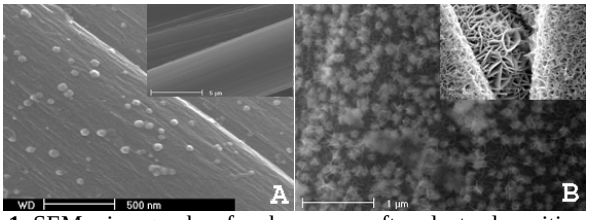

Figure 1: SEM micrographs of carbon paper after electrodeposition of Co: A) with 0.26 mg/cm^2 Co (inset is bare carbon paper) and B) with 4 mg/cm^2 Co (inset is 20 mg/cm^2 Co).

An important aspect of the MWNTs is the high surface area for subsequent Pt deposition. Considering the fact that small catalyst particles are beneficial for the growth of MWNTs with small diameters (therefore high surface area), a loading of 0.26 mg/cm^2 Co on carbon paper was employed in all of the subsequent experiments.

For the MWNT growth, CVD was employed due to its suitable growth temperature and ease to scale-up.[15] Figure 2 presents the SEM and TEM pictures of the resulting MWNTs after CVD growth using a 0.26 mg/cm^2 Co loading. As shown in Figure 2A, a thin layer of MWNTs covers the carbon paper. The as-prepared MWNTs are wavy with lengths in the micrometer range and diameters in the range of 20 to 40 nm (Figure 2B). Some bright particles on MWNTs can also be observed from Figure 2B, which were identified as Co under electron diffraction x-ray spectroscopy (EDX). The TEM image in Figure 2C shows two MWNTs with outer shell diameters of 30 and 40 nm along with some metal particles present in the inner cavity of the MWNTs. The inner diameters of the MWNTs are about 10 nm.

To obtain a high yield of MWNTs on carbon paper to serve as the Pt catalyst support for fuel cell applications, a higher loading of Co on the carbon paper through repetitions of both Co electrodeposition and subsequent CVD carbon nanotube growth was attempted. However, a higher loading of Co on the substrate caused an increase of Co particle size, and the diameter distribution of MWNTs becomes broader, such as 20-130 nm. Also, repetitions of electrodeposition and CVD carbon nanotube growth resulted in amorphous carbon generation.

Figure 2D shows the SEM image of the Pt electrodeposited on the MWNTs. The average diameter of these particles is about 25 nm. The successful deposition of Pt indicates a good electrical contact between the MWNTs and the substrate.

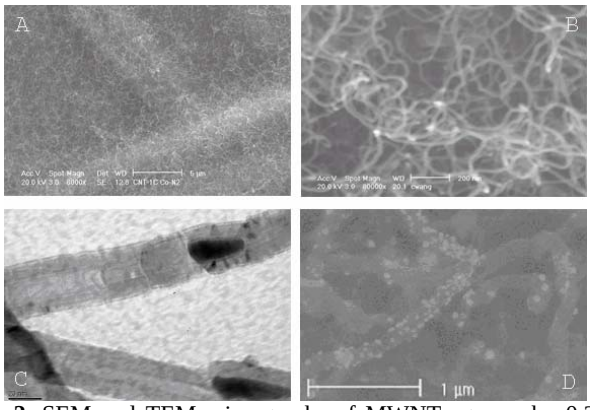

Figure 2: SEM and TEM micrographs of MWNTs grown by 0.26 mg/cm^2 Co loading on carbon paper; A) SEM with low magnification showing high coverage of MWNTs on carbon paper; B) SEM with higher magnification showing the diameter of the MWNTs and presence of Co catalyst particles; C) TEM of MWNTs, D) SEM of Pt particles electrodeposited on MWNTs.

The surface area of the MWNT-carbon paper composite electrode is determined to be in the range between 80-140 m^2/g from nitrogen adsorption by the Brunauer-Emmett-Teller method, while that of carbon paper alone is less than 2 m^2/g. This is consistent with

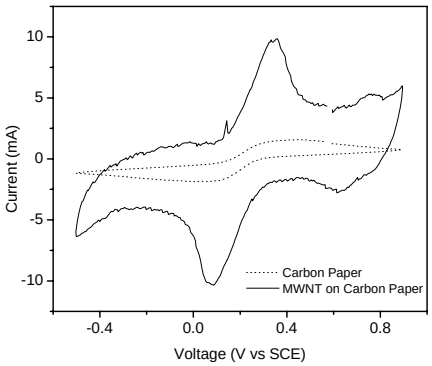

Figure 3: Cyclic Voltammetry in a $K_3Fe(CN)_6$ solution (5 mM $K_3Fe(CN)_6$ + 0.5 M K_2 SO_4) of: 1) 3.46 cm^2 of carbon paper alone; 2) MWNTs grown by 0.26 mg/cm^2 Co loading covering the same 3.46 cm^2 carbon paper. Scan rate: 50 mV/s.

what we have obtained from cyclic voltammetry (CV) measurements in potassium ferricyanide (III) solution (Figure 3) where the redox current is much higher for the MWNT-carbon paper composite, further indicating that MWNTs are electrically connected to the carbon paper substrate

Figure 4 shows the performance of the MEA prepared with thee MWNT-carbon paper composite electrodes. Although the performance of the CNT based fuel cell is still lower than that of the conventional PEMFC with comparable Pt loading, the feasibility of our design involving electrodeposition of catalyst for MWNT growth directly on the carbon paper and subsequent electrodeposition of Pt on the MWNTs is demonstrated. It is expected that once the yield and diameter of the MWNTs and the Pt particle sizes are optimized, the carbon nanotube based fuel cell will show superior performance. Work on the optimization of the MWNT loading and nanotube dimensions, as well as on the decrease of Pt particle size, is under way in order to ultimately achieve a high performance PEMFC.

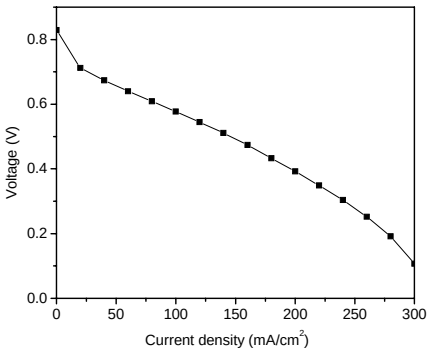

Figure 4: Polarization curve of a MEA prepared by electrodeposition of Pt on MWNTs grown by 0.26 mg/cm^2 Co loading. Pt loading on both electrodes: 0.2 mg/cm^2. Membrane: Nafion 115. Operating conditions: cell temperature, 70°C; humidifier temperature, 80°C; pressure, 2 atm.

Acknowledgement: This work is supported by Pacific Fuel Cell Corporation, UC-Discovery Grant, and California Energy Commission.

References:

(1) Toda, T.; Igarashi, H.; Uchida, H.; Watanabe, M. *J. Electrochem. Soc.* **1999,** *146*, 3750.
(2) Springer, T. E.; Zawodzinski, T. A.; Gottesfeld, S. *J. Electrochem. Soc.* **1991,** *138*, 2334.
(3) Cleghorn, S.J.C.; Ren, X.; Springer, T.E.; Wilson, M.S.; Zawodzinski, T.A.; Gottesfeld S. *Int. J. Hydrogen Energ.* **1997,** *22*, 1137.
(4) Service, R. *Science* **2002,** *296*, 1222.
(5) Srinivasan, S.; Velev, O. A.; Parthasarathy, A.; Manko, D. J.; Appleby, A. J. *J. Power Sources* **1991,** *36*, 299.
(6) Li, W.Z.; Liang, C.H.; Qiu, J.S.; Zhou, W.J.; Han, H.M.; Wei, Z.B.; Sun, G.Q.; Xin, Q. *Carbon* **2002,** *40*, 787.
(7) Li, W. Z.; Liang, C.H.; Zhou, W.J.; Qiu, J.S.; Zhou, Z.H.; Sun, G.Q.; Xin, Q. *J. Phys. Chem. B* **2003,** *107*, 6292.
(8) Liu, Z.L.; Lin, X.H.; Lee, J.Y.; Zhang, W.D.; Han, M.; Gan, L.M. *Langmuir* **2002,** *18*, 4054.
(9) Saito, R.; Fujita, M.; Dresselhaus, G.; Dresselhaus, M.S. *Appl. Phys. Lett.* **1992,** *60*, 2204.
(10) Dresselhaus, M.S.; Hishi, R.A.; Dresselhaus, G.; Inomta, D.; Nakao, K.; Saito, R. *Mol. Cryst. Liq. Cryst. Sci. Tech., Sect. C: Mol. Mater.* **1994,** *4*, 27.
(11) Kasumov, A.Y.; Bouchiat, H.; Reulet, B.; Stephan, O.; Khodos, II.; Gorbatov, Y.B.; Colliex, C. *Eurphys. Lett.* **1998,** *43*, 89.
(12) Smiljanic, O.; Dellero, T.; Serventi, A.; Lebrun, G.; Stansfield, B.L.; Dodelet, J.P.; Trudeau, M.; Désilets, S. *Chem. Phys. Lett.*, **2001,** *342*, 503
(13) Sun, X.; Stansfield, B.L.; Dodelet, J.P.; Désilets, S. *Chem. Phys. Lett.* **2002,** *363*, 415.
(14) Iwasaki, T; Motoi, T.; Den, Y. *Appl. Phys. Lett.*, **1999,** *75*, 2044.
(15) Li, W.Z.; Wang, D.Z.; Yang, S.X.; Wen, J.G.; Ren, Z.F. *Chem. Phys. Lett.* **2001,** *335*, 141.
(16) Yuan, Z. H.; Huang, H.; Dang, H. Y.; Cao, J. E.; Hu, B. H.; Fan, S. S. *Appl. Phys. Lett.* **2001,** *78*, 3127.
(17) Thompson, S.D.; Jordan, L.R.; Shukla, A.K.; Forsyth, M. *J. Electroanal. Chem.* **2001**, *515*, 61.

.

A RELIABLE METHOD FOR THE DETERMINATION OF HYDROGEN STORAGE CAPACITY AT HIGH PRESSURE AND ITS APPLICATION TO CARBON MATERIALS

James M. Blackman, John W. Patrick, Colin E. Snape

Nottingham Fuel & Energy Centre,
School of Chemical, Environmental and Mining Engineering (SChEME), University of Nottingham, University Park, Nottingham NG7 2RD, United Kingdom,
enxjmb@nottingham.ac.uk

Introduction

In recent years, activated carbons, carbon nanofibers and carbon nanotubes have all attracted considerable attention as potential hydrogen storage materials.[1-3] However, determining the hydrogen storage capacity of these materials at high pressure (>10 MPa) has been found to be problematic due to difficulties with reliability and obtaining a satisfactory degree of accuracy.

Primarily, there are two methods that are applied to directly study hydrogen storage capacity of solid materials at high pressures, gravimetric and volumetric. The gravimetric method determines the hydrogen storage capacity of a material by measuring the change of weight of a sample during an adsorption-desorption cycle. The experiments are carried out with *ca* 10 mg of sample in custom built thermo-gravimetric apparatus, which have a high pressure balance chamber.[4] However, this technique is sensitive to all gases sorbed as in principle, it is only based on weighing and this problem is magnified by the very small sample size used for each experiment so is best suited to materials that have high hydrogen storage capacities.

The volumetric method determines the hydrogen storage capacity of a material by measuring the pressure drop resulting from adsorption after exposing the sample to hydrogen at constant volume. This method has the advantage that the conditions are similar to that of a storage tank. Most of the work reported using this method has been carried out using direct pressure measurement in customer built rigs based on the Sieverts type apparatus which is used to determine the hydrogen storage capacity of metal hydrides.[5] However, at high pressures, the Sieverts type apparatus is very sensitive to temperature instability, leaks and additional pressure effects caused by expanding the hydrogen from the reservoir to the sample cell. Recently a second volumetric method has been introduced using a differential pressure method in an attempt to minimise many of these problems.[6]

The difficult nature of the determination of hydrogen storage capacity of a material has contributed to the inconsistencies that have arisen in this field. The reported values for hydrogen storage capacity for carbon materials range from <0.1 wt% for activated carbons, graphite, nanofibers and nanotubes to ~65 wt% for carbon nanofibers.[7,8]

Recognising the difficulties encountered in measuring the adsorption of hydrogen at high pressure, a volumetric differential pressure method has been developed to improve the accuracy of the determination of the hydrogen storage capacity of carbon materials at pressures of *ca*. 10 MPa to a limit of detection of 0.1 wt%. This method has been applied to a series of carbon nanofibers and activated carbons and their adsorption characteristics have been compared.

Experimental

Materials The carbon nanofibers were prepared by carbon vapor deposition from a series of copper-nickel catalysts using ethylene-hydrogen (1:4) as the reactive gas.

The catalyst precursors were prepared by co-precipitation from stoichiometric aqueous solutions of nickel nitrate hexahydrate and iron nitrate nonahydrate using sodium hydroxide solution as the base. Sodium hydroxide was selected over weaker bases used previously to give better definition on precipitation. The resulting suspension was then filtered and the precipitate dried at 107 °C for 24 hours. The product was then calcined at 400 °C for 4 hours to afford the mixed metal oxide catalyst precursor. The catalyst precursor was then finely ground and 50 mg placed in a horizontal quartz reactor tube and reduced for 16 hours under a hydrogen gas flow (100 ml/min) at 450 °C. The reactor then was heated to 600 °C under inert atmosphere. The ethylene-hydrogen (60:240 ml/min) reaction gas was passed over the catalyst for 3 hours. The resulting nanofibers were cooled to room temperature under an inert atmosphere. The carbon nanofibers received no further treatment before adsorption analysis.

The activated carbons used are commercially available and were used with no further treatment.

Adsorption Analysis The nitrogen BET surface area measurements were carried out on an ASAP 2010 and the hydrogen adsorption measurements were made on a custom built volumetric differential pressure apparatus (Figure 1).

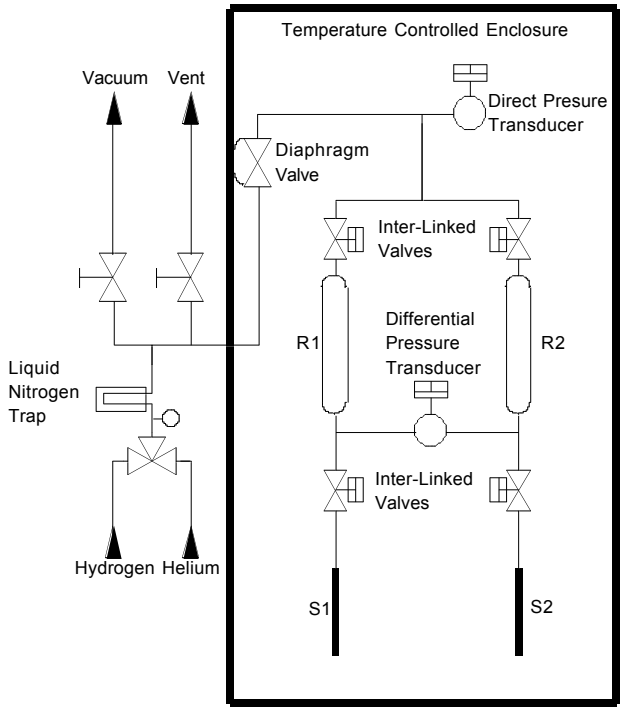

R1 and R2 are reservoir 1 and 2 respectively
S1 and S2 are sample cell 1 and 2 respectively

Figure 1. Schematic of the volumetric differential pressure hydrogen adsorption apparatus

The limb R1+S1 is symmetrical to the limb R2+S2 and the differential pressure transducer has a ±5 bar operational range so that both S1 and S2 can be used as the sample cell. The following protocol is used to operate the apparatus. Using S1 as the sample cell and S2 as the blank, the sample (1-2.5 g) is loaded into S1 and sealed to the apparatus by a high pressure o-ring fitting. The free space in S1+R1 is then determined by helium free space analysis using the differential pressure cell relative to vacuum. The whole apparatus is then evacuated to 0.2 Pa and S1 heated to

150 °C for 2 hours. The heating to S1 is then switched off and the enclosure is then allowed to equilibrate at the operating temperature of 30 °C. The lower inter-linked valves (air-actuated high pressure bellows valves) are then closed. Helium is then admitted to the desired pre-expansion pressure. The top interlinked valves are then closed isolating the limbs and the apparatus isolated by closing the diaphragm valves. The experiment then commences by opening the lower inter-linked valves. After 7 hours the experiment is stopped. The experimental procedures are then repeated using hydrogen.

Results and Discussion

Apparatus The volumetric differential pressure hydrogen adsorption setup has several advantages over the more traditional Sieverts apparatus. Differential pressure transducers have much higher accuracy than direct pressure transducers and by applying the equation of state equation the hydrogen adsorption capacity can be calculated solely using the differential pressure measurement.

$$A = \frac{\Delta PVM_H}{50RTm_C} \quad (1)$$

A=Hydrogen adsorbed (wt%)
M_H=Relative atomic mass of hydrogen
m_c=Mass of sample

The differential pressure system also helps to minimise the errors resulting from minor temperature fluctuations (*ca* ±0.1 °C) of the equipment as R1+S1 and R2+S2 are affected by the same conditions. To prove this, the apparatus was pressurised to 100 bar and both the differential pressure gauge and direct pressure gauge were monitored (Figure 2). The direct pressure reading fluctuated systematically and correlated with the minor temperature changes but the differential pressure reading remained level throughout.

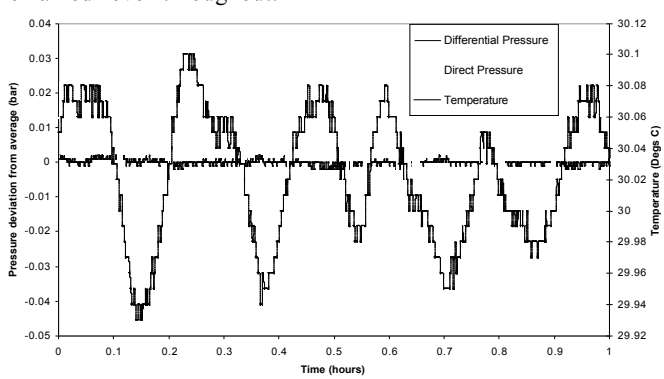

Figure 2. The effect of minor changes in temperature on differential pressure and direct pressure recorded on the volumetric differential pressure hydrogen adsorption apparatus at 10 MPa

The helium run prior to the hydrogen adsorption run acts as a leak detection test. After three hours, all disturbances caused by the expansion of the R1 and R2 into S1 and S2 respectively have returned to equilibrium, so any change in pressure can only be the result of a leak. The helium run is also used as a baseline correction for the hydrogen adsorption run. The initial expansion causes gas at over 11 Mpa to be expanded through a tiny port to a vessel initially at vacuum. This is believed to have a cooling effect on the gas in both limbs, which is dominant in the blank limb as the blank sample cell has more void space to be filled. The result is the pressure is slightly reduced on the blank limb side relative to the sample limb, which is corrected quickly as the apparatus returns the gas to equilibrium pressure. Therefore, the baseline correction is required to give the differential pressure reading an adsorption free reference point; reducing error caused temperature expansion effects and other non-adsorption related phenomena. Without the correction an exaggerated hydrogen adsorption measurement can be observed with and inaccurate profile recorded (Figure 3). This result exaggeration becomes more pronounced with poorer hydrogen adsorbents as the cooling effect becomes increasingly dominant over the adsorption. The true adsorption profile is also lost if a correction is not carried out.

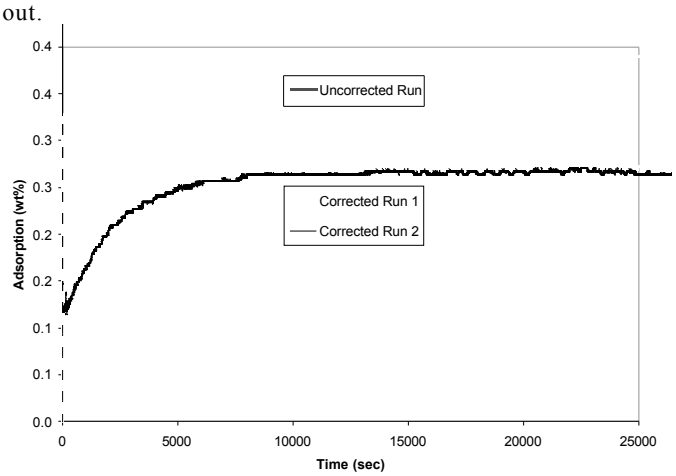

Figure 3. Hydrogen adsorption profile at 10 MPa of carbon nanofibers grown from Cu-Fe-Ni (5:85:10) showing measurement reliability and the error observed if the run is not baseline corrected

The apparatus is guarded from slow leaking through the valves by using low leak rate valves and a pressure buffer between the top inter-linked valves and the diaphragm valve, which is maintained at 5 bar above the operating pressure. The use of 1-2.5 g of sample for a run also enhances the sensitivity of the apparatus, as this is larger than most previous measurements made, which tend to use below 1 g, this ensures that the measurement taken is representative of the sample. The repeatability of the measurements made on volumetric differential pressure hydrogen adsorption apparatus has been found to be excellent. This can clearly be seen for the corrected run 1 & 2 for carbon nanofibers grown from Cu-Fe-Ni (5:85:10).

Adsorption on Carbons As stated a series of activated carbons and carbon nanofibers were analysed for BET nitrogen surface area. The carbon nanofibers were also analysed by XRD and confirm their graphitic nature.

Carbon Nanofibers	Activated Carbons
Fe-Ni (1:9)	Fisher FDC
Fe-Ni (2:8)	Fisher Charcoal FGA
Fe-Ni (3:7)	Norit FGD
Fe-Ni (4:6)	Speakman
Fe-Ni (5:5)	1526-r-98
Fe-Ni (6:4)	1523-r-98
Fe-Ni (7:3)	
Cu-Fe-Ni (5:85:10)	

Table 1. Carbons used for adsorption experiments

The activated carbons analysed were observed to adsorbed 90+ % of their hydrogen adsorption capacity instantly. This is consistent with physisorption being the dominant mechanism of adsorption.

The carbon nanofibers prepared from bi-metallic catalysts were found to have a much lower adsorption capacity than the activated carbons. The carbon nanofibers were observed to adsorb 50-70 % instantly which is assumed to result from physisorption on the surface of the nanofibers. The remainder of the adsorption occurs on a timescale of *ca* 60 minutes, which is thought to result from the hydrogen penetrating between the graphite layers of the carbon nanofibers.

Most of the carbons studied followed the basic trend of their nitrogen BET surface area showing a broadly linear relationship with their final hydrogen adsorption capacity (Figure 4). However, carbon nanofibers grown from a Cu-Fe-Ni (5:85:10) were observed to adsorb more hydrogen than would be expected relative to the recorded nitrogen BET surface area measurement (circled in Figure 4). This may be the result of hydrogen penetration of the graphitic layers which is inaccessible to nitrogen.

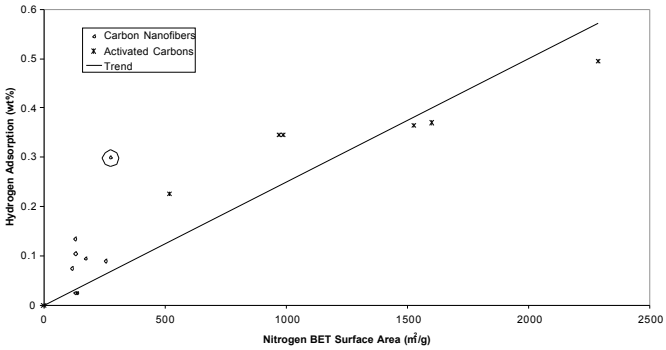

Figure 4. Graph outlining the relation ship between final hydrogen adsorption capacity at 10 MPa of the carbon and the corresponding nitrogen BET surface area values

Conclusions

The volumetric differential pressure hydrogen adsorption apparatus developed has been shown to be reliable and accurate method for determining the hydrogen adsorption capacity of a material to 0.1 wt%. The carbons studied displayed a broadly linear correlation between their hydrogen adsorption capacity and nitrogen BET surface area. However, certain carbon nanofibers did deviate from this trend to be favorable towards hydrogen. If carbon nanofibers do have the potential to adsorb large amounts of hydrogen it would appear that their structure is critical.

Acknowledgement The work was supported by Air Products and Chemicals, Inc. and the EPSRC research council. We gratefully acknowledge the technical advice from Dr. G. Pez (Air Products and Chemicals, Inc.), Mr. F. Anderton and Mr. M. Fletcher and the XRD analysis carried out by Mr. D. A. Clift.

References

(1) Cheng, H. M.; Yang, Q. H.; Liu, C. *Carbon* **2001**, *39*, 1447-1454.
(2) Zuttel, A.; Sudan, P.; Mauron, P.; Kiyobayashi, T.; Emmenegger, C.; Schlapbach, L. *Int. J. Hydrog. Energy* **2002**, *27*, 203-212.
(3) Darkrim, F. L.; Malbrunot, P.; Tartaglia, G. P. *Int. J. Hydrog. Energy* **2002**, *27*, 193-202.
(4) Strobel, R.; Jorissen, L.; Schliermann, T.; Trapp, V.; Schutz, W.; Bohmhammel, K.; Wolf, G.; Garche, J. *J. Power Sources* **1999**, *84*, 221-224.
(5) Fan, Y. Y.; Liao, B.; Liu, M.; Wei, Y. L.; Lu, M. Q.; Cheng, H. M. *Carbon* **1999**, *37*, 1649-1652.
(6) Browning, D. J.; Gerrard, M. L.; Lakeman, J. B.; Mellor, I. M.; Mortimer, R. J.; Turpin, M. C. *Nano Lett.* **2002**, *2*, 201-205.
(7) Tibbetts, G. G.; Meisner, G. P.; Olk, C. H. *Carbon* **2001**, *39*, 2291-2301.
(8) Chambers, A.; Park, C.; Baker, R. T. K.; Rodriguez, N. M. *J. Phys. Chem. B* **1998**, *102*, 4253-4256.

Dynamic Measurement of Hydrogen Storage/Release Properties Using Tapered Element Oscillating Microbalance for Mg Doped with Nano-sized Pd Catalyst

Xiaochun Xu, Jian Zheng and Chunshan Song*

Clean Fuels and Catalysis Program, The Energy Institute, and Department of Energy & Geo-Environmental Engineering, The Pennsylvania State University, 209 Academic Projects Building, University Park, PA 16802, USA

* Contact E-mail: csong@psu.edu; Fax: 814-865-3248

Introduction

Hydrogen storage is one of the key enabling technologies for the advancement of hydrogen power systems, such as fuel cells, in transportation, stationary, and portable applications. For practical application, a reliable measurement of hydrogen absorption/release data is important for the proper design of hydrogen storage devices.

Three different techniques, i.e., volumetric method,[1] gravimetric method[2] and thermal desorption spectroscopy (TDS)[3], have been applied for studying the hydrogen storage/release in solids. The volumetric method measures the pressure drop owing to hydrogen absorption after applying a hydrogen pressure to the specimen contained in a constant volume. Similarly the pressure increase or gas blow off due to desorption can be measured. For volumetric measurement, one has an accumulation of the error. Furthermore, any leakage or temperature instability of the apparatus may give rise to large experimental errors. The gravimetric method measures the weight changes of the specimen due to absorption or desorption of hydrogen. However, data obtained by the gravimetric method are influenced by effects associated with flow patterns, bypassing, and aerodynamic factors such as buoyancy. Gas flow rate smaller than 100 ml/min is required for a reliable measurement.[4] Furthermore, this technique is not sensitive to the nature of gasses absorbed or desorbed since it is only based on weighing. At high temperature or high pressure, the mass resolution of the gravimetric apparatus is significantly reduced. In addition, the response time is 10 to 30 sec, which is not suitable for short duration and kinetics study. Thermal desorption spectroscopy (TDS) measures only the hydrogen desorption in high vacuum utilizing mass spectrometry.

In our laboratory, we are using a technique called tapered element oscillating microbalance (TEOM), where the solid sample is examined as a packed bed, through which the gas passes through. This technique circumvents most of the above problems associated with volumetric method, gravimetric method or TDS.

The main feature of the TEOM technique is an oscillating element that is based on inertial forces, instead of weight, to measure the amount adsorbed. Therefore, errors associated with leakage, flow patterns, bypassing, and aerodynamic factors can be eliminated. Mass resolution of TEOM is also not reduced at higher temperature and high pressure. Consequently, TEOM allows accurate and reproducible measurements. In addition, the fast response time up to 0.1 second makes the short-residence-time measurement and kinetic study possible and reliable. However, there is little literature report on the measurement of hydrogen absorption/release in metal hydride by TEOM.

In this paper, hydrogen storage/release properties of magnesium and palladium-doped magnesium were investigated by using the TEOM technique. The hydrogen storage/release data measured by TEOM were compared with those of measured by the volumetric method.

Experimental

An integrated flow system designed on the basis of a Rupprecht & Patashnick TEOM 1500 pulse mass analyzer (100-mg sample volume) was used for measurement of hydrogen storage and release properties. The active element of the TEOM consists of a tube constructed of a material having a special taper. A feedback system maintains the oscillation of the tapered tube. The natural frequency will change in relation to the mass in the tapered tube. The mass uptake is then determined by the change of the oscillating frequency. The mass uptake is then determined by the change of the oscillating frequency through equation 1.[5]

$$\Delta M = K_0\left(\frac{1}{f_1^2} - \frac{1}{f_0^2}\right) \qquad (1)$$

where ΔM is the weight change, K_0 is spring constant, f_0 is oscillation.

A simplified diagram of the oscillating element is shown in Figure 1. Gases are fed to the unit using Brooks mass flow controllers. The total pressure in the oscillating element is controlled by a backpressure controller. Quartz wool was used at the top and the bottom of the sample bed to keep the hydrogen storage materials firmly packed, which is essential for the stable measurement. Both the feed gas and purge gas was hydrogen and both the feed gas and purge gas flow rate was 100 ml/min. About 30 mg sample was used in the measurements. A detailed description of the TEOM apparatus is available in the literature.[5,6]

Samples used in this paper are magnesium (Aldrich, 99.8%, 325 mesh) and palladium nanoparticle-doped magnesium. The nanoparticle palladium-doped magnesium was prepared by an in-situ catalyst deposition method.[7] The hydrogen absorption was carried out at 573 K and 400 psi. The hydrogen release was measured at 613 K and ambient pressure.

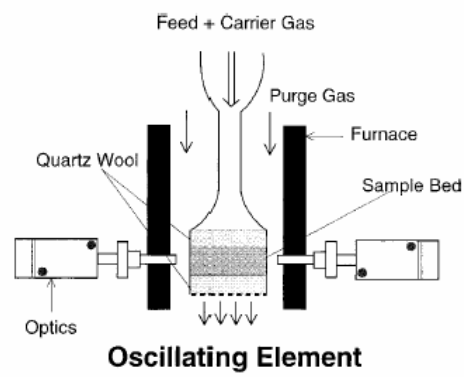

Figure 1. Simplified diagram of the oscillating tapered element with a sample bed.

Results and Discussions

1. Hydrogen absorption measurement

The hydrogen absorption performance of Pd-doped magnesium were measured by TEOM and compared with that measured by volumetric method in our previous study.[7] Figure 2 compares the hydrogen absorption properties of Pd-doped magnesium measured by TEOM and volumetric method at 573 K under 400 Psi. The hydrogen storage capacity measured by TEOM is almost the same as that measured by volumetric method, which indicates the accuracy of the two measurement methods. However, the hydrogen absorption rate measured by TEOM is faster than that measured by the volumetric method. When the hydrogen absorption is measured by volumetric method, the Pd-doped magnesium is sealed in a vessel with high pressure hydrogen gas. Therefore, the hydrogen storage is carried out

in static status and hydrogen concentration gradient exists in the adsorption bed, which results in the slow mass transfer in the absorption bed and slow hydrogen absorption rate. On the other hand, when the hydrogen absorption is measured by TEOM, a high flow rate forces hydrogen gas flow through the adsorption bed, which improves the mass transfer in the adsorption bed and accelerates the hydrogen absorption rate. Another important feature is that the response time for TEOM is very fast, as short as 0.1 second, whereas the response time for the volumetric method is very long. TEOM makes the fast measurement and kinetic study possible and reliable. Chen et al[6] also reported that TEOM provided more accurate data on the catalyst deactivation kinetics than the conventional microbalance.

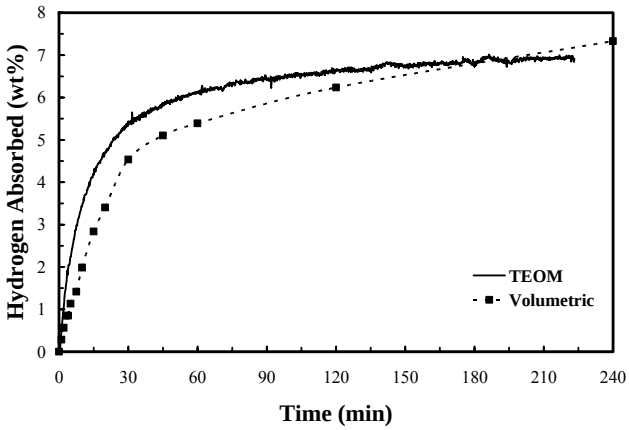

Figure 2. Comparison of hydrogen absorption properties of Pd-doped magnesium measured by TEOM and volumetric method at 573 K and under 400 Psi.

2. Hydrogen release measurement

The hydrogen release properties of Pd-doped magnesium were also measured by TEOM and compared with that measured by volumetric method in the previous study.[7] Figure 3 compares the hydrogen release properties of Pd-doped magnesium measured by TEOM and volumetric method at 613 K and atmosphere pressure. Similarly, the hydrogen release rate measured by TEOM is also faster than that measured by the volumetric method. Due to the elimination of hydrogen concentration gradient in the adsorption bed and the fast response time of TEOM, TEOM provides a more accurate and detailed information on the hydrogen absorption and release kinetic than the volumetric method or other gravimetric methods, which is important for the design of next generation high performance hydrogen storage materials and for the proper design of hydrogen storage devices in practical application.

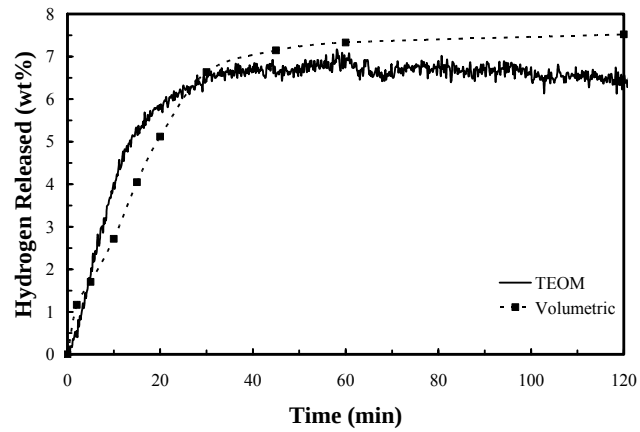

Figure 3. Comparison of hydrogen release properties of Pd-doped magnesium measured by TEOM and volumetric method at 613 K and under ambient pressure.

3. Effect of nano-sized Pd catalysts on hydrogen release

The effect of nanoparticle palladium catalysts on the hydrogen release properties of magnesium hydride was measured by TEOM at 613 K and under ambient pressure and the results are shown in Figure 4. Apparently, the rate of hydrogen release for palladium-doped magnesium hydride is much faster than that for the un-doped magnesium hydride, which is in consistent with that of measured by volumetric method.[7] While the Pd-doped magnesium readily releases hydrogen, the un-doped magnesium needs 5 minutes of incubation time before it releases hydrogen. At 10 minutes, the magnesium hydride and Pd-doped magnesium hydride releases 0.76 wt% and 4.03 wt% hydrogen, respectively. After 40 minutes of hydrogen release, Pd-doped magnesium hydride almost releases all the absorbed hydrogen and the un-doped magnesium hydride only releases about 50% of the absorbed hydrogen.

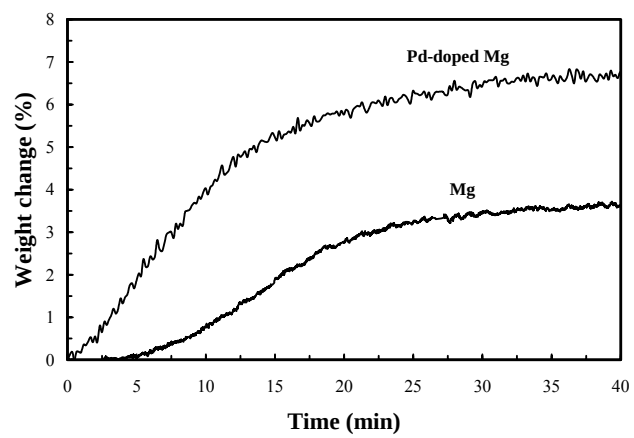

Figure 4. Effect of nanoparticle palladium catalysts on the hydrogen release properties of magnesium measured by TEOM at 613 K and under ambient pressure.

Conclusions

TEOM provides a dynamic, and more accurate information on the hydrogen absorption and release kinetics than the volumetric method or other gravimetric methods, which is important for the design of next-generation high-performance hydrogen storage materials and for the proper design of hydrogen storage devices in practical application.

Acknowledgement. Financial support from the Hydrogen Energy Center at the Pennsylvania State University in the form of a Seed Grant is highly appreciated.

References

(1) Bogdanoviæ, B.; Sandrock, G. *MRS Bulletin* **2002**, 712.
(2) Ströbela, R.; Jörissena, L.; Schliermannb, T.; Trappc, V.; Schützd, W.; Bohmhammele, K.; Wolfe, G.; Garchea, J. *Journal of Power Sources* **1999**, *84*, 221.
(3) Dillon, A. C.; Jones, K. M.; Bekkedahl, T. A.; Klang, C. H.; Bethune, D. S.; Heben, M. J. *Nature* **1997**, *386*, 377.
(4) Patashnick, R., TEOM measurement, Personal Communication.
(5) Zhu, W.; Graaf, J. M. v. d.; Broeke, L. J. P. v. d.; Kapteijn, F.; Moulijn, J. A. *Industrial Engineering Chemical Research* **1998**, *37*, 1934.
(6) Chen, D.; Gronvold, A.; Rebo, H. P.; Moljord, K.; Holmen, A. *Applied Catalysis A: General* **1996**, *137*, L1.
(7) Xu, X. C.; Song, C. S. *Preprints of Symposia - American Chemical Society, Division of Fuel Chemistry* **2003**, *48*, 941.